

Sara Patricia Pereira Couto

Metallurgical characterization of 3D-printed metal components

Metallurgisk karakterisering av 3D-printede metallkomponenter

Master's thesis in Master of Science in Materials Technology Engineering (MSMT)

Supervisor: Nima Razavi

Co-supervisor: Saveria Spiller

June 2023

Sara Patricia Pereira Couto

Metallurgical characterization of 3D-printed metal components

Metallurgisk karakterisering av 3D-printede metallkomponenter

Master's Thesis for the Degree of Master of Science in Materials Engineering

Supervisor: Nima Razavi

Co-supervisor: Saveria Spiller

June 2023

Norwegian University of Science and Technology

Faculty of Natural Sciences

Department of Materials Science and Engineering



ABSTRACT

Additive manufacturing offers a promising method for creating intricate shapes using different materials, with steel components typically used for high-strength applications due to their great strength and fatigue resistance. However, the initial cost of equipment and production makes additive manufacturing for metal expensive. A novel technique called Material Extrusion Additive Manufacturing has recently been proposed to address this issue.

This master thesis aims to explore the potential of producing stainless steel 316L using the MEAM technique while maintaining mechanical properties comparable to conventionally manufactured specimens. The study involves printed specimens using a composite filament composed of 316L powder particles and a polymer binder, with subsequent post-processing steps, such as debinding and sintering, are required to obtain the final printed parts. The project encompasses the production of specimens, characterization of the printed product, material analysis, and mechanical testing.

The mechanical properties of the printed specimens obtained through the MEAM process demonstrate room for improvement, highlighting a knowledge gap in understanding the influence of process parameters on porosity, density, microstructure, and resulting mechanical properties.

By conducting a comprehensive analysis of particle size distribution, surface roughness, defects and porosity distribution, grain size, microhardness, finite element simulations, fracture tests, tensile testing and fractography, valuable insights are gained into the mechanical behavior of the printed specimens. The findings indicate opportunities for optimizing printing parameters, and material characteristics to improve the mechanical properties, such as strength, ductility, and load-bearing capacity of the printed stainless steel 316L parts.

SAMMENDRAG

3D-pinting tilbyr en lovende metode for å skape komplekse former ved bruk av ulike materialer, der stålkomponenter typisk brukes i applikasjoner som krever høy styrke på grunn av deres store styrke og motstand mot utmattelse. Imidlertid gjør de innledende kostnadene for utstyr og 3d-printing produksjon av metall kostbar. En innovativ 3d-printingsteknikk har nylig blitt foreslått for å adressere denne utfordringen.

Denne masteroppgaven har som mål å utforske potensialet for å produsere rustfritt stål 316L ved bruk av MEAM-teknikken samtidig som mekaniske egenskaper som er sammenlignbare med konvensjonelt produserte prøver opprettholdes. Studien innebærer 3d-printede prøver ved bruk av et komposittfilament bestående av 316L-pulverpartikler og et polymerbindemiddel. Med etterfølgende videre avbinding og sintring, er nødvendige for å oppnå de endelige 3d-printede delene. Prosjektet omfatter produksjon av prøver, karakterisering av det 3d-printet produktet, materiellanalyse og mekanisk testing.

De mekaniske egenskapene til de 3d-printede prøvene oppnådd gjennom MEAM-prosessen viser et potensial for forbedring, og peker på et kunnskapsgap når det gjelder å forstå innvirkningen av prosessparametere på porøsitet, tetthet, mikrostruktur og resulterende mekaniske egenskaper.

Ved å gjennomføre en omfattende analyse av prøveforberedelse, partikkelstørrelsesfordeling, overflate-ruhet, defekter og porøsitetsfordeling, kornstørrelse, mikrohardhet, endelige element-simuleringer og trekktesting, oppnås verdifulle innsikter i den mekaniske atferden til de 3d-printede prøvene. Funnene indikerer muligheter for å optimalisere printeparametere og materielle egenskaper for å forbedre de mekaniske egenskapene, som styrke, duktilitet og bæreevne til de 3d-printede rustfrie stål 316L-deler.

PREFACE

This master's thesis marks the culmination of my academic journey in the field of Material Science and Engineering at NTNU. Conducted at the Department of Mechanical and Industrial Engineering, as a continuation of my specialization project in TMM4560, submitted in December of 2022.

I would like to express my sincere gratitude to my main supervisor, Professor Nima Razavi, for entrusting me with the opportunity to engage in this exciting research, even though we had not crossed paths previously to the specialization project. His leap of faith and belief in my abilities have been instrumental in my growth throughout this project. Nima's valuable insights have played a pivotal role in shaping this thesis.

I am also immensely grateful to Ph.D Candidate Saveria Spiller, who has been an incredible mentor and source of knowledge. Countless hours have been spent together in the laboratory, where Saveria's unwavering commitment and her remarkable knowledge have greatly contributed. Saveria has created an environment of comfort and trust, encouraging me to ask even the most seemingly simple questions related to the tests. This thesis stands as a testament to Saveria's exceptional guidance and support.

Lastly, I am profoundly grateful to my parents, whose belief in my aspirations and support have been instrumental in my academic journey. Their enduring trust in my choices and unwavering encouragement to explore unorthodox paths have shaped the person I am today. I am truly fortunate to have them by my side.

CONTENTS

Abstract	i
Preface	iii
Contents	vi
List of Figures	vi
List of Tables	viii
Abbreviations	xi
1 Introduction	1
1.1 Motivation and Scope of Work	1
1.2 Background: MEAM and FDM	3
1.2.1 Filament	4
1.3 The Process	7
1.3.1 The Printing Phase	7
1.3.2 Debiding and Sintering	8
2 Theory	9
2.1 Mechanical Properties and Characterization of 316L MEAMed Parts	9
2.1.1 316L	9
2.1.2 Effect of Printing Parameters on the Mechanical Properties .	12
2.1.3 Effect of Printing on the Materials Microstructure	13
2.1.4 Parameters Affecting Properties	15
3 Material and Methods	19
3.1 Specimen Fabrication	19
3.1.1 Dogbone specimens	20
3.1.2 3-Point Bending Specimens	21

3.2	Experimental Procedures	23
3.2.1	Particle Size Measurement	23
3.2.2	Surface Roughness Evaluation	24
3.2.3	Grain Size Measurement	25
3.2.4	Microhardness - Vickers	26
3.3	Tensile Tests	28
3.3.1	Apparatus	29
3.4	3-Point Bending Tests	29
3.4.1	Finite Element Simulations	29
3.4.2	Tests Procedures	31
3.5	Fractography	34
4	Results	35
4.1	Specimen Preparation	35
4.2	Particle Size Measurement	37
4.3	Surface Roughness Evaluation	38
4.4	Defects and Porosity Distribution	39
4.5	Grain Size Measurement	40
4.6	Microhardness - Vickers	41
4.7	Finite Element Simulations	43
4.8	Tensile Test	45
4.9	Fracture Tests	47
4.9.1	Compliance Test	47
4.9.2	Basic Procedure	48
4.10	Fractography	50
4.10.1	Dogbone Fractured Surface	50
4.10.2	Etching on 3-Point Bending Fractured Surface	52
4.10.3	SEM of 3-Point Bending Fractured Surface	53
5	Discussions	55
5.1	Specimen Preparation	55
5.2	Particle Size Measurements	56
5.3	Surface Roughness Evaluation	56
5.4	Defects and Porosity Distribution	57
5.5	Grain Size Measurement	58
5.6	Microhardness - Vickers	59
5.7	Finite Element Simulations	59
5.8	Tensile Tests	60
5.9	Fracture Tests	61
5.9.1	Compliance Test	61

5.9.2 Basic Procedure	62
5.10 Fractography	65
6 Conclusions	67
6.1 Further Work	72
References	73
Appendices:	80
A Particle Size Measurements	81
	82
B Roughness Evaluation	83
	83
C Microhardness - Vickers	86
	86
D Simulations	89
	89

LIST OF FIGURES

1.2.1 Process illustration [4].	3
2.1.1 A typical stress-strain curve for a ductile material demonstrates the relationship between tensile stress-strain. σ_y represents the yield point, σ_f is the yield strength, and σ_u the ultimate tensile strength. Σ is the equivalent strain for the same points. [33]	10
2.1.2 Stress-strain curves obtained with 316L dogbone specimens, printed using MEAM in previous work by the research group [34].	10
2.1.3 Comparison of microstructures between sintered 316L (equiaxed) and SLM-processed 316L (anisotropic). The image illustrates the distinct grain morphology and directional properties induced by different additive manufacturing techniques [42].	14
2.1.4 a 90° angle for horizontally printed and upright specimens, b 45° angle for horizontally printed, c 0° raster angles for horizontally printed, and e 45° and f 0° build orientation for vertically printed bending, taken from [46].	16
2.1.5 Cross-sectional sketches illustrating the variations in infill structure size for specimens in [47]. The outlines of four layers were consistent, while the hexagonal infill structure underwent size reduction across different specimens: (a) Infill Degree (ID) 25; (b) ID 50; (c) ID 75; (d) ID 100 [47].	18
3.1.1 Cuboid Dimensions i mm, with a thickness of 12 mm, presented in Figure 3.1.3.	19
3.1.2 Schematic representation of the dogbone specimens after extraction in mm.	20
3.1.3 Front section of the cuboid in mm, from which two single edge notch specimens are cut.	21
3.1.4 Notch size R=0.25, blue, the measures are in mm.	21

3.1.5 Notch size R=0.50, yellow, the measures are in mm.	22
3.1.6 Notch size R=1.00, green, the measures are in mm.	22
3.1.7 Color reference on cuboids.	22
3.2.1 Vickers indentation [58].	26
3.2.2 Schematic of both laying and standing Vickers specimen as presented in Figure 3.2.3.	27
3.2.3 Points where the values were taken, equal for both Flat Top and Vertical Back specimens.	27
3.3.1 Image of fixture in [60].	28
4.1.1 Cutting of Dogbone specimens.	35
4.1.2 Dogbone specimen after cutting and painting.	36
4.1.3 Cutting Of 3-Point Bending Specimens.	36
4.2.1 Embedded filament.	37
4.2.2	37
4.3.1 Bar plot of average roughness Ra in μm on the two surfaces tested for each cuboid, the detailed values for the averages can be found in chapter B.	38
4.3.2 Surface tested on the cuboids.	38
4.4.1 Defects and porosity distribution representation on flat specimens.	39
4.4.2 Defects and porosity distribution representation on vertical specimens.	39
4.5.1 A) 100 μm scale and B) magnification in 20 μm	40
4.5.2 A) 100 μm scale and B) magnification in 20 μm	40
4.6.1 Vickers microhardness indentation example, scale 0.1 mm.	41
4.6.2 Microhardness data of both specimens.	42
4.7.1 Sketch of simulation.	43
4.7.2 Boundary condition and loading applied.	43
4.7.3 Mesh on simulation.	44
4.8.1 Stress-Strain plot for the specimens tested with Tensile test.	46
4.9.1 Flat specimens.	48
4.9.2 Vertical specimens.	48
4.9.3 R0.25	48
4.9.4 R0.50	48
4.9.5 R1.00	48
4.10.1 Etched crack, scale 500 μm	52
4.10.2 Magnified etched crack, scale 200 μm	52
4.10.3 Magnified etched surface, scale 100 μm	52

LIST OF TABLES

3.1.1 Printing parameters for cuboids.	20
4.1.1 Notch size on specimens taken from Vertical Front for illustrative proposes, scale bar: 1 mm.	36
4.6.1 H2.0 Average Values on Flat Top specimens, measured in micrometers.	41
4.6.2 H2.0 Average Values on Vertical Back Specimen, measured in mi- crometers.	41
4.7.1 Kt values from simulations in $\text{MPa}\sqrt{\text{mm}}$	44
4.8.1 Tensile specimens with their respective printed orientation.	45
4.8.2 DIC before/after fracture images of T1 for illustrative purposes. . .	45
4.8.3 Ultimate Tensile Strength for each specimen.	46
4.9.1 Load values of the basic procedure curves.	49
4.9.2 Average indicative fracture toughness values for each notch size. . .	49
4.10.1 Before and after visual representation of specimen T1, scale 1.000 mm.	50
4.10.2 Before and after visual representation of specimen T2, scale 1.000 mm.	50
4.10.3 Before and after visual representation of specimen T3, scale 1.000 mm.	51
4.10.4 Before and after visual representation of specimen T4, scale 1.000 mm.	51
4.10.5 SEM on Vertical Front Specimens.	53
4.10.6 SEM on Vertical Back Specimens.	53
4.10.7 SEM on Flat Front Specimen.	54
4.10.8 SEM on Flat Back Specimens.	54
A.0.1 Particle Size Measurements in micrometers.	82
B.0.1 Roughness Values, measured in micrometers.	83

B.0.2	Roughness 3D image example for illustration purposes - 5 measures taken in different positions of the top of the cuboid printed flat number 1. The evaluation length used was 2.5 mm per each measure.	84
B.0.3	Roughness Graphs example for illustration purposes - Cube F2. . .	85
C.0.1	Vickers values on Flat Top Specimen, measured in micrometers. . .	87
C.0.2	Vickers values on Vertical Back Specimen, measured in micrometers.	88

ABBREVIATIONS

- **ABS** Acrylonitrile Butadiene Styrene
- **AM** Additive Manufacturing
- **CAD** Computer-Added Design
- **CMOD** Crack Mouth Opening Displacement
- **DIC** Digital Image Correlation
- **FDM** Fused Deposition Modeling
- **FFF** Fused Filament Fabrication
- **MEAM** Material Extrusion Additive Manufacturing
- **PETG** Polyethylene Terephthalate Glycol-Modified
- **PLA** Polylactic Acid
- **TPE** Thermoplastic Elastomer
- **TPS** Thermoplastic Styrenic Block Copolymer
- **3PB** 3-Point Bending

INTRODUCTION

1.1 Motivation and Scope of Work

As a Material Science and Engineering student, my fascination with the potential of additive manufacturing to revolutionize the manufacturing industry has only grown stronger over time. The ability to create intricate shapes using different materials has the potential to not only improve efficiency and reduce waste but also usher in a new era of product design and manufacturing.

However, despite its many advantages, the high cost of equipment and production has limited the widespread use of additive manufacturing for metal components. This has led to a particular interest in the Material Extrusion Additive Manufacturing (MEAM) technique and its potential to reduce the cost of producing high-strength steel components using 3D printing.

Stainless steel 316L stands out among the various materials due to its widespread use in the manufacturing industry and its excellent mechanical properties. Exploring the potential of MEAM for producing stainless steel 316L with comparable mechanical properties to conventionally manufactured specimens can help bridge the knowledge gap in the influence of process parameters on mechanical properties.

This master's thesis represents a unique opportunity to apply knowledge and skills toward the development of cost-effective and sustainable manufacturing processes. As an aspiring engineer, the goal is to make a positive impact in the manufacturing industry and contributing to the development of innovative solutions that can help shape the future of manufacturing.

The thesis comprises several chapters that delve into various aspects of the research. As an introduction, chapter 1, provides an overview of the subject matter, research objectives, and the significance of the study. A short and comprehensive

literature review on Fused Deposition Modeling (FDM) is presented, exploring its principles, applications, and advancements in the field. Moving forward, chapter 2, focuses on the theoretical framework, offering an in-depth analysis of the mechanical properties of 316L stainless steel. In chapter 3 the methods and apparatus employed in conducting the tests and experiments conducted for this thesis are outlined, ensuring transparency and replicability. The subsequent chapter, chapter 4, showcases the results obtained from the conducted tests, offering detailed analysis and interpretation. The chapter 5, also engages in a comprehensive discussion of the findings, highlighting their implications and potential avenues for future research in the form of Further Work. In chapter 6, the thesis concludes with a concise summary of the key findings, reiterating their significance and contribution to the field. Additionally, the appendix, located after Chapter 6, section 6.1 contains supplementary materials such as tables and images that enhance the understanding and support the content presented throughout the thesis.

1.2 Background: MEAM and FDM

Material extrusion additive manufacturing (MEAM) is a revolutionary 3D printing technique that involves the extrusion of material layer by layer to create a 3D object. The process uses a computer-controlled extrusion nozzle that deposits successive layers of material onto a build platform, which can be used to create complex custom objects that are challenging or impossible to produce using traditional manufacturing methods [1].

Fused Deposition Modeling (FDM) is a type of MEAM that has gained popularity for its versatility and cost-effectiveness. This process involves heating and extruding a thermoplastic or composite filament, through a moving print head to create the desired shape. By depositing layers of material, the print head can move in three dimensions and create intricate designs. FDM is an intriguing and innovative manufacturing technique that has the potential to produce an array of products, including prototypes, models, and functional end-use parts [2] [3].

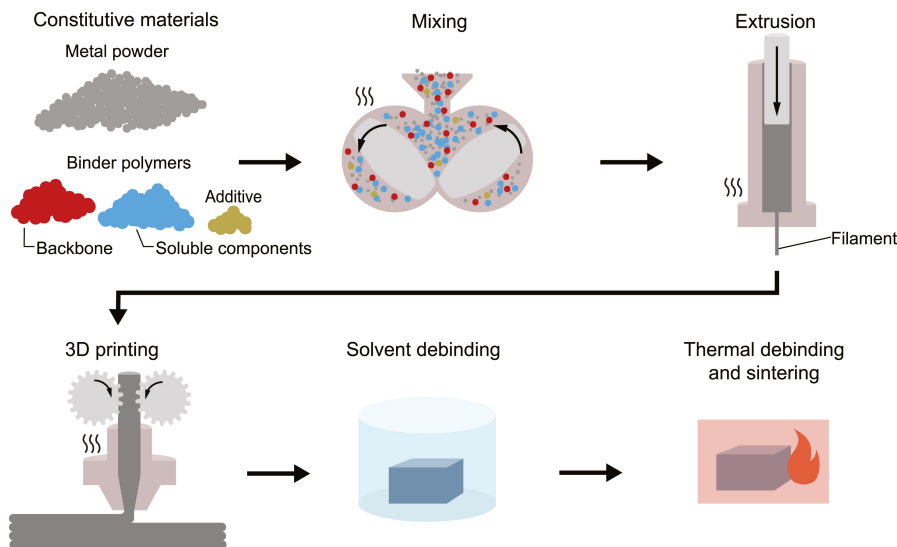


Figure 1.2.1: Process illustration [4].

MEAM is the adaption of FDM to metal production because the filament is composed of a polymeric matrix and metal powder dispersed in it section 1.2.1. MEAM consists of three phases. The first phase involves the extrusion of the metal filament in an FDM printer, moreover in section 1.2.1 , resulting in a green part made of a powder and binder system. The specimens then undergo a debinding process to remove the polymeric binder, creating a brown part. Finally, the packed metal powder undergoes a sintering process where the powder bonds together as a result of a thermal cycle. For metallic filaments, debinding and sintering are part of the post-operation process. The final product is often referred to as the "silver part"

at the end of the three phases [5] [6].

MEAM has the potential to revolutionize metal manufacturing by enabling the creation of complex objects with unprecedented precision and flexibility. Its applications are extensive and range from aerospace and automotive industries to biomedical engineering and consumer products [3][7][8].

1.2.1 Filament

Filament-based 3D printing technologies, including FDM, are based on the extrusion of a thin and lengthy strand of material called a filament, fed into the nozzle. The extrusion nozzle then melts the filament and deposits it layer by layer onto the build platform, forming the final product. Filaments used in FDM can be made from a diverse range of materials, such as ABS, PLA, and PETG [9] [10].

Filament-based FDM, also known as Fused Filament Fabrication (FFF), is widely used due to its safety, simplicity, and affordability. As mentioned before, MEAM typically involves a two-component filament composed of high-consistency metal powder dispersed in an organic multi-component binder polymer. This method enables the production of metal parts using a 3D printer, which eliminates the need for costly and time-consuming metal casting or machining processes [8].

The type and volume fraction of metallic powder content in the filament plays a critical role in determining the final printed part's density, mechanical properties, and tribological properties. Studies have shown that an increase in the volume fraction of metal powder typically leads to an increase in the density of the printed part. The composition of the metal powder and binder can be challenging to balance, as seen in the case of PLA and Ni-Cu gas-atomized powders used for feedstock production [8] [3] [11].

In order to achieve the desired properties of the printed parts, it is essential to carefully consider the volume fraction and type of metallic powder content used in the filament. Researchers have explored various approaches to improve the mechanical and physical properties of 3D-printed metal parts. For example, a study conducted by Chawla et al. in 2021 found that adding graphene nanoplatelets to copper filament can significantly enhance the mechanical properties of the printed parts, including an increase in strength, stiffness, and toughness [12].

1.2.1.1 Powder Fraction

Regarding material extrusion techniques like FDM, there are a few options for feedstock, including filament, pellets, and rods. While filament-based extrusion is common, pellet-based extrusion has a few advantages. It requires less pre-processing and uses a vertical single-screw extruder with feeding ports and heaters, which makes it more efficient overall. In contrast, rod-based extrusion involves using a plunger to push feedstock to the nozzle, which can lead to lower accuracy during the start and end of the printing process [13] [14] [15].

The powder fraction, a key parameter that represents the proportion of powder to binder material within the filament, holds significant influence over the properties and characteristics of the final product. This pivotal factor allows manufacturers to finely tune the powder fraction, enabling the creation of a diverse array of products with distinct densities and mechanical attributes. Within the realm of MEAM, an assortment of metal powders, such as aluminum, cobalt, nickel, stainless steel, and titanium-based alloys, is commonly employed. These materials exhibit exceptional strength, corrosion resistance, and robustness when transformed into intricate parts [16] [17]. Noteworthy options like stainless steels 316L and 17-4 PH are favored due to their exceptional weldability, while Ti-6Al-4V stands out for its remarkable biocompatibility, garnering acclaim in the realm of medical applications [18].

A recent study conducted by Magnus Wagner in 2022 revealed that the filament's composition can significantly affect its properties, especially the binder strength and feedstock rheology, [4]. Wagner's research gradually replaced TPE with PE70 in the feedstock mixture and discovered that the binder strength increased, but the filament became more brittle and prone to failure during mechanical testing. Additionally, the feedstock's rheology was observed to decrease in viscosity and stress levels for higher values of PE70. These findings emphasize the importance of carefully controlling the powder fraction to guarantee the desired properties and characteristics of the final product [19] [20] [19] [21] [22] [23].

1.2.1.2 Binder

The binder material is a critical component of the MEAM process, serving as the adhesive that binds the powder particles together to form the desired filament. A typical binder composition comprises three main components: the primary material, the backbone, and various additives, with the proportions of each component determining the green part quality and thus the final properties of the printed specimens [4]. The primary material refers to the main substance that constitutes the

binder composition. It is responsible for providing the adhesive properties required to bind the powder particles together during the MEAM process. The selection of the primary material depends on the specific application requirements, such as the desired strength, flexibility, or other desired characteristics of the printed specimens. The backbone component serves as the structural foundation of the binder material. It imparts stability and strength to the composition, ensuring that the printed filament maintains its shape and integrity during the extrusion process. The backbone contributes to the overall mechanical properties of the printed specimens, such as tensile strength, elongation, and impact resistance. Additives are supplementary components included in the binder composition to enhance specific properties or functionalities. These additives can impart desirable traits such as improved adhesion, reduced shrinkage, increased flexibility, enhanced thermal stability, or even specific chemical or mechanical properties. The selection and proportions of additives are carefully determined to achieve the desired characteristics in the final printed specimens [24].

In recent research, the minimum amount of backbone polymer required for stable binders was investigated. In a study conducted in 2021, the backbone polymer fraction in a binder containing soluble TPE and PE3 backbone polymer was gradually reduced in each experiment. The results showed that specimens began to crack during the debinding process when the backbone polymer fraction was below 7.5 vol.%, highlighting the importance of the proper balance of components in binder composition [25] [11].

Poly(lactic acid) (PLA) is a popular binder material due to its biodegradability, ease of processing, and good mechanical strength, despite its high brittleness. However, researchers in a different study found that a composite filament of TPS and PLA exhibited lower toughness, making it less cost-effective. To improve the filament's mechanical properties, they added a chain extender, resulting in an increase in both melting temperature and cold crystallization temperature [25].

In addition, a research group explored the use of various granulometric expanded perlite microspheres and the percentage amount in an Acrylonitrile Butadiene Styrene (ABS) composite filament. They found that the printing process was significantly influenced by the filler content, with a maximum percentage of 20, producing a fine perlite filament with thermal insulating properties. These findings demonstrate the potential for incorporating different types of filler materials in binder compositions to achieve unique filament properties [26] [27].

1.3 The Process

The process to obtain the final 3D printed parts consists of three distinct phases, each requiring precise control of various parameters and considerations. These phases are essential in achieving the desired properties and functionality of the final components. In the following sections, each phase is individually presented, and its specific parameters and factors.

1.3.1 The Printing Phase

The printing phase begins with feeding the filament into a rotating feed roller and pushing it towards the nozzle. This process involves heating the filament above its melting point, which is a critical parameter as discussed in subsection 2.2. The feedstock is then extruded from the nozzle and deposited layer by layer onto the bed to create the desired object or specimen. However, some parts may require a support structure, which needs to be manually removed [8].

The printing process requires the use of a G-code, which is generated by slicing the 3D CAD model of the part using software such as Cura. The software also determines the path that the printer will follow while setting other printing parameters such as the printing angle and layer thickness [8] [28].

Several studies have explored the optimization of the 3D printing process of metal powder. For example, researchers have investigated the effects of nozzle temperature, layer height, and printing speed on the microstructure and mechanical properties of printed metal parts. It was found that adjusting these parameters can significantly impact the final quality of the printed part, with higher nozzle temperatures resulting in improved densification and strength, while lower layer heights lead to better surface finish and improved fatigue resistance.

In another study, Sun et al. (2020) investigated the effect of different nozzle diameters, layer thicknesses, and printing temperatures on the mechanical properties of stainless steel 316L parts printed using FDM. They found that changing the nozzle diameter and layer thickness can significantly impact the mechanical properties of the printed part, with smaller nozzle diameters and layer thicknesses resulting in improved mechanical properties. The researchers also found that increasing the printing temperature led to an increase in the elongation at break and a decrease in the ultimate tensile strength of the printed parts [29].

Lu et al. (2021) developed a new feedstock material with a higher packing density, resulting in improved mechanical properties and reduced porosity in the final printed part. They demonstrated that their feedstock could achieve a tensile strength of 607 MPa, which is higher than the typical range of 400-500 MPa for 316L stainless steel printed using FDM [27].

1.3.2 Debiding and Sintering

Powder-based manufacturing methods, such as MEAM, require two key processes: debinding and sintering.

Debinding and sintering are critical processes in the 3D printing of metal components, and their optimization is essential to achieve the desired final properties.

Debinding

Debinding involves removing the binder material from the 3D-printed object, leaving only the powder particles behind to prepare it for sintering. This can be achieved through a combination of mechanical, chemical, and thermal processes, including thermal debinding, which involves heating the part to a high temperature using a chemical solvent or catalytic processes. The temperature ranges from 60 to 600°C, and stable temperature is required for a specific duration to produce a brown part. The size, accuracy and porosity of the final object are affected by the debinding process [17]. For example, studies have shown that the debinding temperature can affect the degree of shrinkage in the final part, with lower debinding temperatures resulting in higher shrinkage [4] [30].

Sintering

Sintering is the process of heating the debound powder particles to a high temperature, below the melting point, to fuse them together and create a solid, fully-dense, and homogeneous object. During sintering, surface, lattice, and grain boundary diffusion, as well as other mass transfer mechanisms, occur. The sintering temperature, time, and atmosphere can significantly impact the final microstructure, density, and mechanical properties of the component [31] [30].

Researchers have found that the sintering process affects the final object's shrinkage, with parameters such as the sintering atmosphere, heating rate, and sintering time playing a crucial role. For example, a study conducted by Dayue Jiang in 2022 found that plate shrinkage on the side was larger than on the horizontal direction, possibly due to gravity during sintering [8]. Additionally, post-sintering treatments such as heat treatment, hot forging, or rolling can be employed to enhance the final mechanical properties or tailor the microstructure to specific applications. Moreover, surface finishing post processes play a crucial role in additive manufacturing. These processes involve various techniques such as polishing, grinding, sanding, or chemical treatments to improve the surface quality, texture, and appearance of the printed components. Surface finishing can also be used to achieve specific functional properties like corrosion resistance, wear resistance, or biocompatibility, depending on the desired application [30].

2.1 Mechanical Properties and Characterization of 316L MEAMed Parts

This section explores the underlying principles and theories governing the mechanical properties of 316L MEAMed parts, including aspects such as tensile strength, hardness, ductility, and fracture toughness. Additionally, it highlights the characterization methods employed to evaluate these properties, providing a comprehensive understanding of the material behavior and performance of 316L stainless steel parts produced through MEAM.

2.1.1 316L

316L is classified as austenitic stainless steel that boasts a distinctive composition, making it highly resistant to sensitization and intergranular corrosion. This can be attributed to its low carbon content, which enhances its mechanical properties, including higher strength and ductility. The steel's microstructure is typically composed of austenitic grains with a face-centered cubic structure, while small quantities of ferrite can be induced via cooling or mechanical deformation.

The typical tensile strength of 316L ranges from 485 to 620 MPa, with a corresponding yield strength of 170 to 310 MPa. This high tensile strength indicates the material's ability to withstand significant mechanical loads and stresses. Furthermore, 316L demonstrates notable elongation values, with elongation at break ranging from 40% to 60%, indicating its capacity to deform plastically before failure [32]. Ideally, stress-strain curves for ductile materials look like Figure 2.1.1. In the curve, the absorbed Strain Energy Density (SED) gradually accumulates

within the material until reaching the point of final fracture [33]. The Figure 2.1.2 plot represents the tensile test results obtained from Sondre Olsøybakk Kolstad's Master's thesis titled 'Structural Integrity of AISI 316L Fabricated via Material Extrusion Additive Manufacturing' [34]. In his thesis, dogbone-shaped tensile specimens were directly 3D-printed on a horizontal orientation, also named flat. The process parameters are the same used to print the specimens used in the present work. This is presented later on in chapter 3.

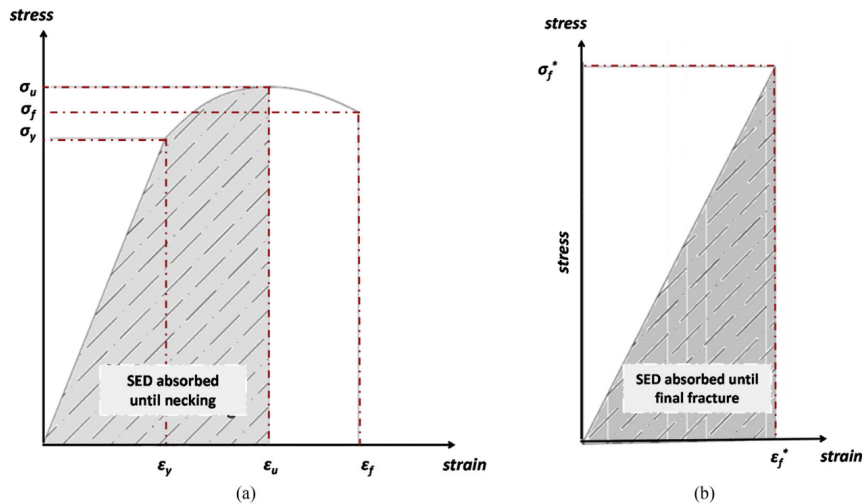


Figure 2.1.1: A typical stress-strain curve for a ductile material demonstrates the relationship between tensile stress-strain. σ_y represents the yield point, σ_f is the yield strength, and σ_u the ultimate tensile strength. Σ is the equivalent strain for the same points. [33]

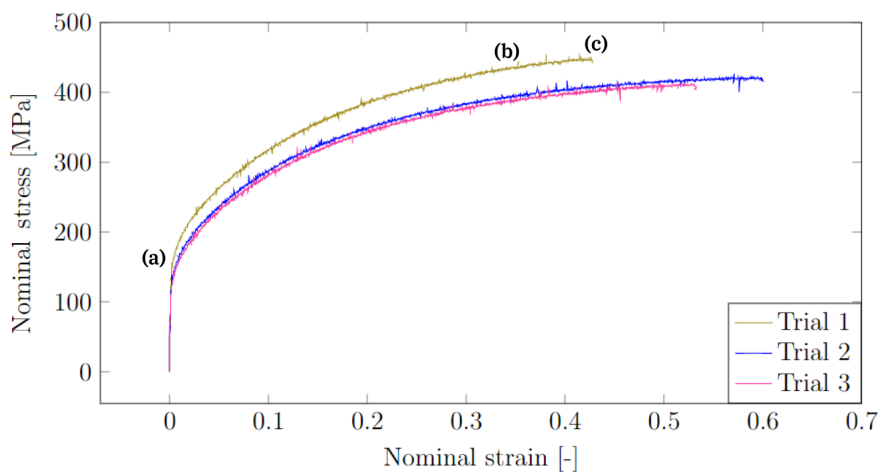


Figure 2.1.2: Stress-strain curves obtained with 316L dogbone specimens, printed using MEAM in previous work by the research group [34].

The Figure 2.1.2 plot displays the relationship between nominal stress and nominal strain for three different trials of tensile testing. Initially, all specimens exhibit linear elastic behavior, where stress and strain are directly proportional. The endpoints of the graphs indicate the fracture points of the specimens, marking the point at which the material fails under the applied load.

The Vickers hardness of 316L typically ranges from 170 to 220 HV. This hardness value indicates that the material is relatively hard and can withstand moderate wear and tear [32].

The composition of 316L consists of various elements, including carbon (ranging from 0 to 0.03%), chromium (16 to 18%), iron (61.9 to 72%), manganese (0 to 2%), molybdenum (2 to 3%), nickel (10 to 14%), phosphorus (0 to 0.045%), sulfur (0 to 0.03%), and silicon (0 to 1%). These elements contribute to the unique properties of 316L, including its high resistance to sensitization and intergranular corrosion, as well as its excellent mechanical properties [32].

Given its unique properties, 316L is widely used across various industries, including chemical processing, medical implants, and aerospace components. The advent of sintering and 3D printing technologies has further expanded its potential applications, offering new design possibilities and improved material properties. To ensure its quality and reliability, 316L is regulated by various ASTM standards, including ASTM A240 [35], for plate, sheet, and strip, ASTM A269 [36], for seamless and welded tubing, and ASTM A276 [37] for bars and shapes.

When it comes to sintering or 3D printing processes, these can significantly impact the microstructure of 316L. During sintering, the steel is heated to a temperature below its melting point, causing the powders to fuse together through diffusion. This sintered material then undergoes a cooling process to form a solid body, but the microstructure can vary depending on the sintering temperature and time. Studies have shown that increasing the sintering temperature can result in a larger grain size but at the same time, it can help reduce the internal porosity, which is beneficial for the mechanical properties. In general, the typical microstructure of sintered parts is isotropic, characterized by equiaxial grains. Additionally, sintering at higher temperatures can lead to the formation of more intermetallic compounds, which can improve wear and corrosion resistance.

To the contrary, additive manufacturing techniques such as powder bed fusion (PBF) can lead to changes in anisotropic microstructure. The printing process involves depositing layers of metal powders and selectively melting them using a laser or electron beam. This results in the formation of elongated grains along the building direction. The grains are usually small due to the rapid solidification. Research indicates that the mechanical properties are dependent on the printing parameters, such as laser power, scanning speed, and layer thickness. For example,

increasing the laser power can result in larger grains and improved mechanical properties, while decreasing the layer thickness can increase the surface roughness and reduce the mechanical properties.

In terms of mechanical properties, sintered 3D-printed 316L can exhibit comparable or even improved properties compared to conventionally processed 316L. Studies have shown that sintered 316L can have a yield strength of up to 400 MPa and an ultimate tensile strength of up to 700 MPa, depending on the sintering temperature and time. Additionally, sintered 316L can exhibit good wear and corrosion resistance. Similarly, 3D-printed 316L can exhibit a yield strength of up to 550 MPa and an ultimate tensile strength of up to 800 MPa, depending on the printing parameters. The fatigue behavior of 3D-printed 316L has also been studied, with results indicating that the material can exhibit good fatigue resistance [32].

2.1.2 Effect of Printing Parameters on the Mechanical Properties

The mechanical properties of 3D-printed final silver metallic part are critical to their functional performance, and accurately characterizing these properties is essential in guaranteeing that the end product meets the user's requirements [38].

Research has shown that the mechanical properties of a 3D-printed object depend on the printing parameters set in the slicing software, such as the printing angle, layer thickness, fill rate, nozzle size, the melting temperature of the feedstock material, and bed temperature. Additionally, the size of the components may change during the printing process, leading to a need for careful consideration of shrinkage, which can affect the final dimensions of the printed part [38].

To achieve the desired mechanical properties of a 3D-printed object, post-processing techniques such as heat treatment may be required. Heat treatment can help to increase the strength and toughness of the printed part by homogenizing its microstructure and by minimizing porosity. The debinding and sintering processes, which are integral parts of the MEAM process, can also affect the mechanical properties of the printed part. Researchers have found that the silver part experiences shrinkage in both the x- and z-directions after sintering, and the shrinkage in these directions differs due to interlayer gaps [38].

2.1.3 Effect of Printing on the Materials Microstructure

In the case of 316L stainless steel, the microstructure is typically composed of austenite and ferrite phases, which can be modified through the sintering process to achieve specific mechanical properties, aforementioned.

To evaluate the microstructure of 3D-printed and sintered 316L specimens, several techniques can be used, including optical microscopy, scanning electron microscopy (SEM), and X-ray diffraction (XRD). Standards such as ASTM E45 [39], and ASTM E562 [40], provide guidelines for microstructural examination and analysis, and can be useful in characterizing the microstructure of 3D-printed and sintered 316L.

Research by Dayue Jiang has shown that the microstructure of 17-4 PH stainless steel specimens after extrusion additive manufacturing consisted of an austenitic phase with fine carbides and lath martensite within the grains on a BCC plate-lattice structure. While this study focused on a different material, the findings highlight the importance of understanding the microstructure of 3D-printed parts and how it can be modified to achieve specific mechanical properties.

In the case of 316L stainless steel, sintering can alter the microstructure through the formation of intergranular bonding between particles, resulting in densification and grain growth. However, excessive sintering can lead to the formation of coarse grains and the degradation of mechanical properties.

Recent research by X. Zhang et al. showed that the microstructure of 3D-printed and sintered 316L can be optimized through careful control of the sintering parameters. By varying the sintering temperature and holding time, they were able to achieve a microstructure with a fine and uniform grain size, resulting in improved mechanical properties such as higher strength and ductility.

The resulting precipitation-hardening increased surface hardness, although the martensite phase could not be identified on the side surface of the plate-lattice structure. The study also found that irregular sintering can alter the microstructure, leading to faster grain growth on the side surface, and that micropores distributed along the grain boundaries can affect the microstructure. To ensure the quality and reliability of 3D-printed parts, it is important to adhere to industry standards and guidelines that address microstructure and other relevant factors. For example, the ASTM E562 standard [40], specifies methods for analyzing microstructures of metallic materials using optical microscopy, while the ASTM E2119 standard [41], outlines guidelines for the assessment of sintered metal powder materials.

A finer and more uniform microstructure typically results in higher mechanical properties such as strength and stiffness, while a coarser and more inhomogeneous microstructure may lead to lower mechanical strength but higher ductility. There-

fore, it is important to carefully consider the microstructure when designing and manufacturing 3D-printed parts.

The microstructure of 3D-printed and sintered 316L is a complex topic that requires careful consideration of various factors, including sintering parameters, particle size and distribution, and the presence of impurities. By understanding the microstructure and how it can be modified, it is possible to optimize the mechanical properties of 3D-printed parts for specific applications. Sintering of 316L typically results in an equiaxed microstructure, as reported in [42]. In contrast, the SLM process often yields an anisotropic microstructure, characterized by unique directional properties and grain morphology [42].

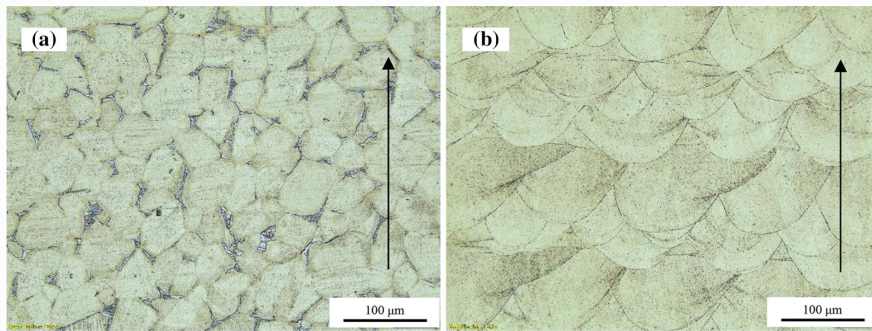


Figure 2.1.3: Comparison of microstructures between sintered 316L (equiaxed) and SLM-processed 316L (anisotropic). The image illustrates the distinct grain morphology and directional properties induced by different additive manufacturing techniques [42].

These differences arise from variations in processing parameters, thermal cycles, and solidification rates, among other factors.

2.1.4 Parameters Affecting Properties

Layer Direction

The direction of the 3D-printed layers, known as the layer direction or building orientation, plays an important role in the mechanical properties of the printed part. Typically, the mechanical properties of a 3D-printed part are higher in the direction perpendicular to the layering direction and lower in the direction parallel to the layering direction. This is because the layers are bonded together through sintering or other means, which affects the strength and stiffness of the printed part. All the parameters involved in the process can affect the mechanical properties and the final outcome quality. Many studies in the literature focus on different aspects of the process. For instance, James Allum and Andrew Gleadall investigated the interlayer interface of standard specimens, which they found to be the reason for anisotropic mechanical properties. They loaded the specimens in both longitudinal (axis of extruded filament) and transverse (interface between the layers) directions. Their microscopic characterizations showed very similar results for both directions, although the longitudinal direction exhibited reduced plasticity, strain-fracture, and load-bearing properties.

Therefore, optimizing the layer direction, layer thickness, and infill patterns can significantly improve the mechanical properties of 3D-printed parts for specific applications [38] [43].

Layer Thickness

The thickness of each layer in the MEAM process is a critical parameter that affects the mechanical properties and overall quality of the final 3D-printed object. Various factors determine the real thickness of the layers, such as the size of the nozzle, the extrusion speed, and the flow rate multiplier set in the slicing software. Researchers have investigated the effects of layer thickness on the mechanical properties of 3D-printed objects. A study by R. Martukovich et al. showed that thinner layers resulted in higher tensile strength and stiffness in the axial direction, while thicker layers produced higher strength in the transverse direction. In another study by K. Kempen et al., it was found that thinner layers could lead to increased ductility and toughness, whereas thicker layers exhibited higher Young's modulus and ultimate tensile strength. However, printing thinner layers may result in higher resolution and better surface finish, but it can also be more challenging to print and require longer printing times. On the other hand, thicker layers can be easier to print and may be more robust, but they can lead

to lower resolution and rougher surface finish. Therefore, determining the optimal layer thickness for a specific application is a crucial step in the MEAM process to achieve the desired mechanical properties and surface finish [44] [38].

Raster Angle

The angle at which material is extruded from the nozzle is a critical aspect of the MEAM process. Typical angles are $+45/-45^\circ$, although 90° is also common. It has a significant impact on the mechanical properties and surface quality of the final product. Research shows that modifying the extrusion angle can strengthen the product, with steeper angles resulting in stronger bonds between the layers and a more robust final product. Conversely, shallower angles can result in weaker bonds and a weaker final product. Moreover, the extrusion angle affects the surface finish of the final product. Steeper angles can result in a rougher finish, whereas shallower angles can provide a smoother finish. Additionally, the extrusion angle affects the dimensional accuracy of the final product, with steeper angles resulting in more shrinkage and distortion and shallower angles leading to less shrinkage and distortion. Numerous studies have investigated these effects, underscoring the need for proper control and optimization of the extrusion angle to achieve high-quality 3D-printed objects [38] [45]. A few raster angles are presented below.

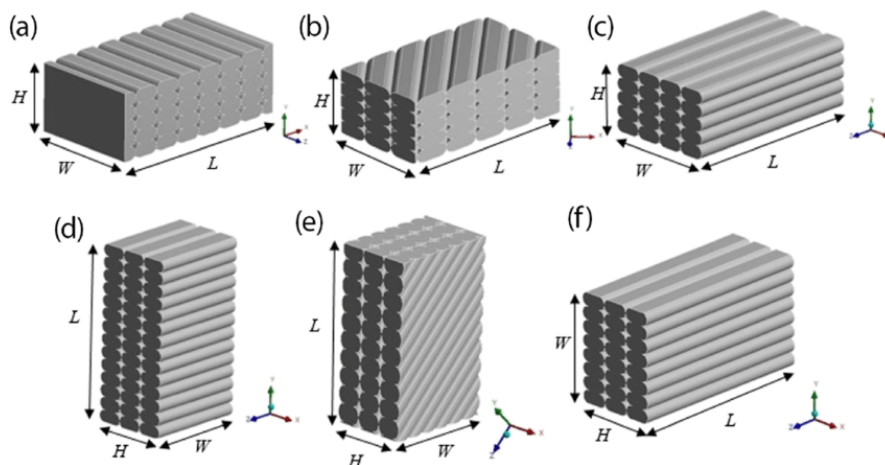


Figure 2.1.4: a 90° angle for horizontally printed and upright specimens, b 45° angle for horizontally printed, c 0° raster angles for horizontally printed, and e 45° and f 0° build orientation for vertically printed bending, taken from [46].

Infill Density

Infill density is a crucial parameter that influences the mechanical properties and overall quality of 3D-printed parts. A study by Gao et al. [17], investigated the effect of infill density on the mechanical properties of PLA specimens produced using fused deposition modeling (FDM). They found that increasing the infill density from 20% to 80% resulted in a substantial increase in flexural and tensile strengths. Additionally, they observed that the failure mode of the specimens shifted from brittle to ductile as the infill density increased. Another study by Ahn et al. [5], explored the relationship between infill density and thermal conductivity of 3D-printed parts. They found that increasing the infill density led to higher thermal conductivity due to the increased density of the material. These findings suggest that infill density is a critical parameter that can be tailored to achieve specific mechanical and thermal properties in 3D-printed parts [38] [45].

Infill density also affects the printing time and cost, as higher densities require more material and longer printing times. Studies have shown that reducing infill density can significantly reduce printing time and material cost while maintaining suitable mechanical properties [20]. Infill density also impacts the surface finish of the final product, with higher densities providing a smoother finish and lower densities resulting in a rougher finish. This effect has been investigated in several studies, where it was found that increasing the infill density resulted in a smoother surface finish due to the increased density of the material. Therefore, selecting the appropriate infill density is essential to achieving the desired mechanical properties, cost-effectiveness, and surface finish of the final 3D-printed object [38] [45].

In the study conducted by Rosnitschek et al.[47], all parts were printed with a shell of four outlines, four top layers, and four solid bottom layers. The remaining volume was filled with a hexagonal honeycomb pattern as the infill structure at infill degree levels of 25%, 50%, 75%, and 100%, as illustrated in [47]. For clarity, we will refer to these configurations as ID 25, ID 50, ID 75, and ID 100. To compensate for sinter shrinkage, the dimensions in the printing plane were scaled by a factor of 1.2, and in the vertical direction, by a factor of 1.26.

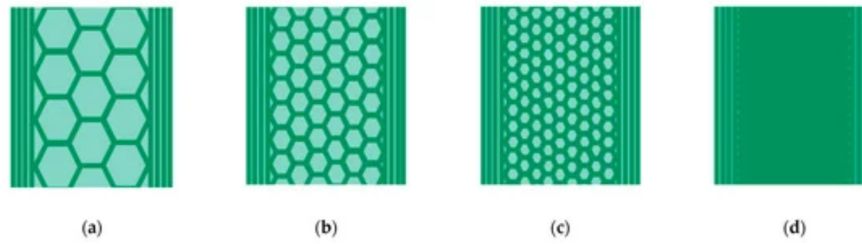


Figure 2.1.5: Cross-sectional sketches illustrating the variations in infill structure size for specimens in [47]. The outlines of four layers were consistent, while the hexagonal infill structure underwent size reduction across different specimens: (a) Infill Degree (ID) 25; (b) ID 50; (c) ID 75; (d) ID 100 [47].

MATERIAL AND METHODS

3.1 Specimen Fabrication

All tests were performed on specimens made from two printed cuboid of the following dimensions,

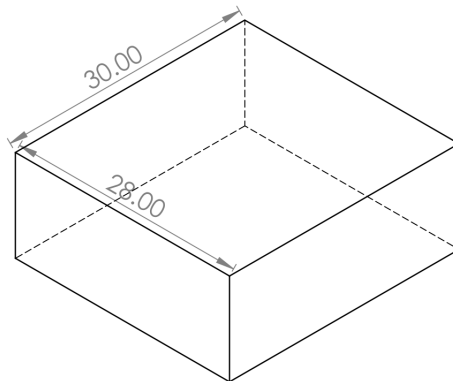


Figure 3.1.1: Cuboid Dimensions i mm, with a thickness of 12 mm, presented in Figure 3.1.3.

These were printed in different orientations: one cuboid was printed vertically, and the other cuboid was printed horizontally, from hereon referred to as flat. The cuboids utilized in this Master Thesis were fabricated prior to the current study by the esteemed research group as referenced in [34]. The printing process employed a Prusa 3D printer [48], in conjunction with the BASF 316L filament, which is detailed in section 1.2.1 [49]. The process parameters of most importance are presented below, for a detailed view on the parameters used, see [34].

Table 3.1.1: Printing parameters for cuboids.

Printing Parameter	Value	Unit
<i>Nozzle Temperature</i>	290	°C
<i>Bed Temperature</i>	110	°C
<i>Printing Speed</i>	30	mm/s
<i>Layer Height</i>	0.1	mm
<i>Cooling Fan Percentage</i>	50	%

3.1.1 Dogbone specimens

The extraction of dogbone specimens using [50], for tensile testing is a crucial step in evaluating the mechanical properties of materials. These specimens are characterized by their distinctive shape resembling a dogbone.

The cuboid is divided into two sections to obtain the desired dogbone shape. Two vertical sections (front and back) are obtained for vertically-printed cuboids, while two flat sections (top and back) are extracted for flat-printed cuboids. From each of these sections, a total of eight specimens are carefully crafted, following the design requirements for the standard [51]. The schematic representation provided below offers a visual reference for understanding the resulting shape of the specimens after cutting.

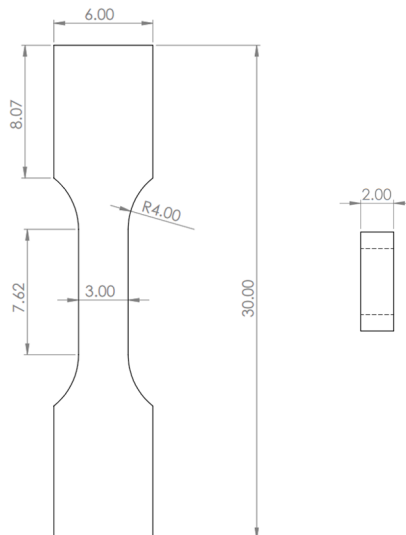


Figure 3.1.2: Schematic representation of the dogbone specimens after extraction in mm.

3.1.2 3-Point Bending Specimens

For the 3-point bending specimens, each cuboid used was cut into two sections using the [50]: two vertical sections (front and back) for the vertically-printed cuboid, and two flat sections (top and back) for the flat-printed cuboid, as shown in Figure 3.1.7.

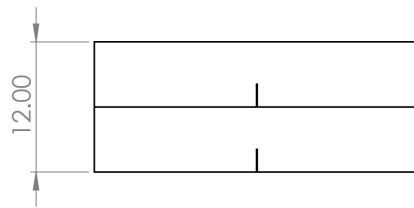


Figure 3.1.3: Front section of the cuboid in mm, from which two single edge notch specimens are cut.

From each of these sections, eight specimens were made obtained, following the design for the three-point bending standard test [52].

3.1.2.1 1 Dimension

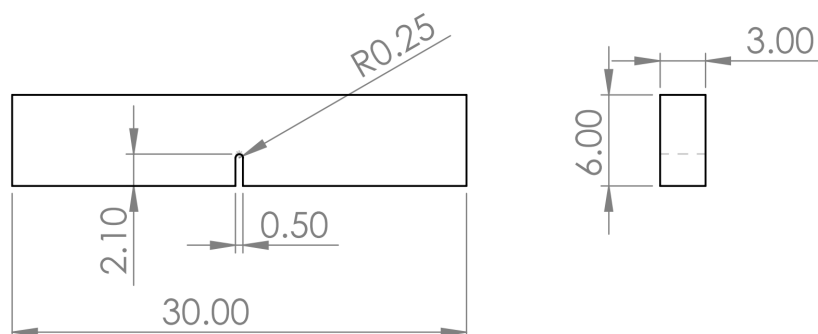


Figure 3.1.4: Notch size $R=0.25$, blue, the measures are in mm.

3.1.2.2 2 Dimension

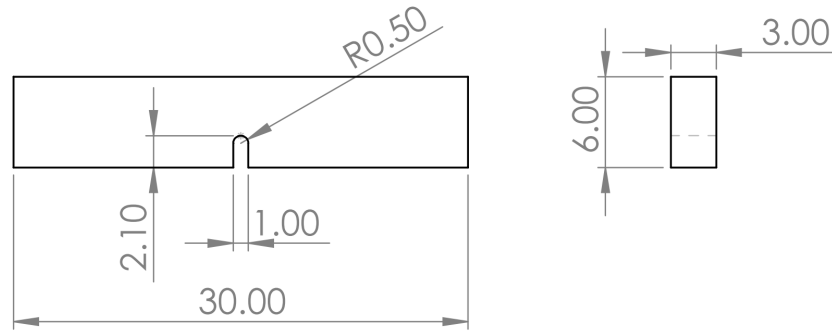


Figure 3.1.5: Notch size $R=0.50$, yellow, the measures are in mm.

3.1.2.3 3 Dimension

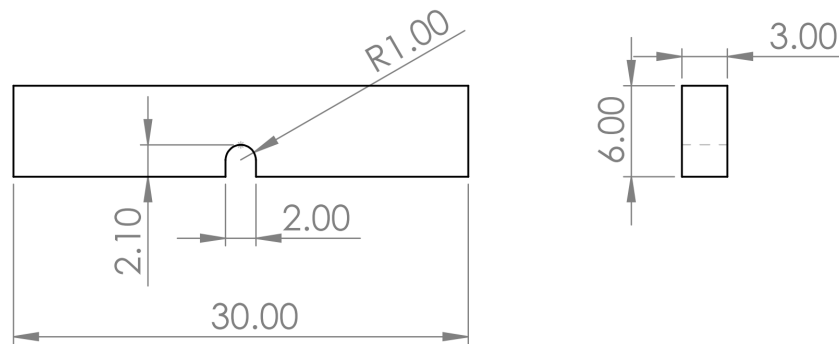


Figure 3.1.6: Notch size $R=1.00$, green, the measures are in mm.

The following cuboid schematic represents the color reference:

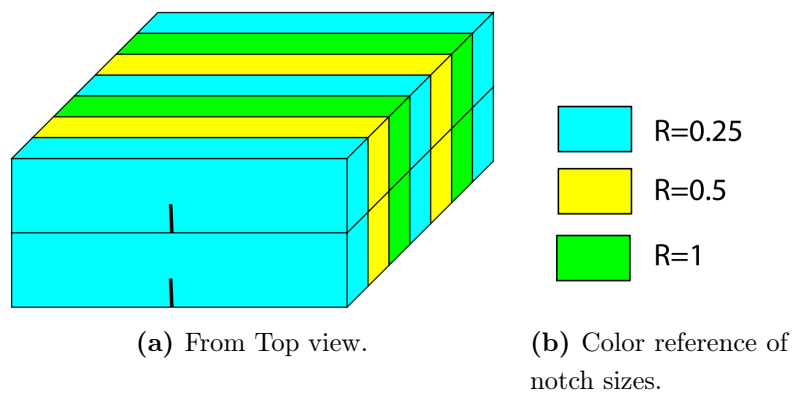


Figure 3.1.7: Color reference on cuboids.

To distinguish the many specimens a color was designated to each notch radius as in 3.1.7b, as this was the only variation. The specimens marked blue can be seen in subsection 3.1.2.1, yellow can be found in subsection 3.1.2.2 and green in subsection 3.1.2.3.

3.2 Experimental Procedures

3.2.1 Particle Size Measurement

In order to measure particle size on the filament, the ClaroCit kit was used to cast a segment of the filament to be able to observe the circular section. The kit consists of a two-part polymer kit that includes a liquid and a powder. The liquid contains methyl methacrylate and tetramethylene dimethacrylate, which are monomers that polymerize to form a solid material. The powder contains a free radical initiator, dibenzoyl peroxide, which is used to initiate the polymerization reaction.

The general process for using the ClaroCit kit is as follows: First, a mold or form is prepared for the desired shape and size of the specimen. Next, the ClaroCit liquid and powder are mixed together according to the manufacturer's instructions, with a specific mixing ratio provided on the packaging or in the product instructions. In this study, a mixing ratio of 10g powder to 6ml liquid was used. The mixture was then poured into the mold or form and allowed to cure and harden according to the manufacturer's instructions. In this study, the ClaroCit was left to cure overnight.

Once the ClaroCit had cured, the specimen was removed from the mold or form. The surface of the specimen was finished as needed using sandpaper and polishing. The particle size of the specimen was then measured using an optical microscope allowing for precise analysis of particle size distribution.

Apparatus

The experiment utilized the Hirox rH-2000 digital microscope (Hirox-USA, Inc., USA) [53], to obtain high resolution images. It has been used to capture the fracture surfaces of the tested specimens as well as to perform roughness tests. The Hirox rH-2000 is a versatile digital microscope that provides high magnification, high resolution, and a range of lighting options to capture images of surface features of materials.

3.2.2 Surface Roughness Evaluation

Roughness testing was performed using a Hirox RH-2000 digital microscope [53]. The surfaces of the cuboids were first cleaned with a soft brush and then placed on the microscope stage. The microscope was set to a magnification of 500x and the camera was focused on the area of interest. A 3D image was then captured using the built-in software. The captured image was then processed using the software to obtain the roughness parameters, including Ra (average roughness), Rz (maximum height of the roughness profile), and Rq (root mean square roughness). 5 measures with equal orientation were taken from two of the sides of each cuboid.

To ensure accuracy, several images were captured from different areas of the sample and the roughness parameters were averaged. The test was performed in triplicate to ensure reproducibility of the results.

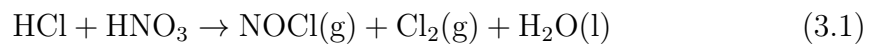
Apparatus

The experiment was conducted employing a Hirox rH-2000, mentioned in section 3.2.1. The Hirox rH-2000 was used to perform roughness testing on the fracture surfaces of the specimens. The roughness tests provided information on the surface quality and characteristics of the materials, allowing for a more in-depth analysis of the fracture mechanisms.

3.2.3 Grain Size Measurement

Etching

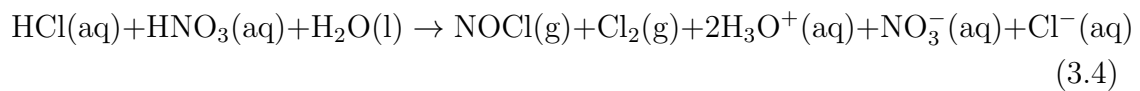
To measure the grain size of a material, an etching process was used in conjunction with an optimal microscope. The etching process involved mixing hydrochloric acid (HCl) [54], and nitric acid (HNO₃) [55], together, which produced nitrosyl chloride (NOCl) as a gas, along with water (H₂O) and chlorine gas (Cl₂), according to the balanced chemical equation:



When this mixture was added to water, the following reactions occurred:



Thus, the overall reaction when the three were mixed together is:



To perform the grain size measurement, the material was first polished to a mirror finish and then etched using this mixture. The etching process reveals the grain boundaries, allowing for the grain size to be measured using an optimal microscope.

Measurement

To determine the grain size of the specimens, the guidelines outlined in standard E112-10 [56], were used, which provides a standardized procedure for performing this analysis.

Specifically, utilizing section 17.5 of the standard, which outlines the procedure for measuring grain size using the linear intercept method. This method involves measuring the number of times a straight line intersects with the boundaries of grains within a microstructure, and then using statistical analysis to calculate the average grain size.

Apparatus

Optical microscopy was performed using the Olympus BX53M optical microscope (Olympus Corporation, Japan) [57]. The Olympus BX53M is a high-quality optical microscope with a wide range of magnification options, making it ideal for examining microstructures and surface features of materials.

3.2.4 Microhardness - Vickers

The Vickers hardness test is a common technique utilized to determine the hardness of various materials, including metals like 316L. The test involves applying a known load for a specified duration of time to the material's surface using a square-based pyramidal diamond indenter. The resulting indentation size is measured using a microscope, as shown in Figure 3.2.1, and the Vickers hardness number (HV) is then calculated using the formula below.

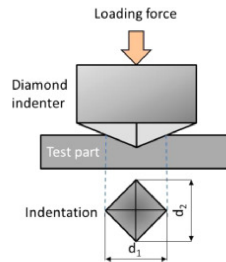


Figure 3.2.1: Vickers indentation [58].

$$HV = \frac{1.854 * F}{d^2} \quad (3.5)$$

[58]

where F is the applied load in Newtons, the constant value **1.854** is a conversion factor derived from the geometry of the Vickers indenter and d is the average of the two diagonals of the diamond indentation in millimeters. This method provides accurate and reproducible results, making it an ideal approach for comparing the hardness of different materials and measuring the effects of various treatments and processing techniques on 316L. The test is performed in accordance with ASTM E384, which provides guidelines for the proper testing procedure, including the load and duration of the indentation.

Microhardness tests are non-destructive and suitable for thin and small samples since the indenter print is shallow. However making it useful for testing materials used in microelectronic devices and other small components. However, the test may be affected by surface roughness, grain size, and other factors that can affect the indentation size and, therefore, the calculated HV value. The specimens were prepared for testing by grinding and polishing to a mirror-like finish. In this study, a load of **2 kgf** was used for the microhardness testing. For this reason, it is advisable to repeat and perform several indentations. In the present work three lines of 10 indentation points, **A**, **B**, and **C**, were created.

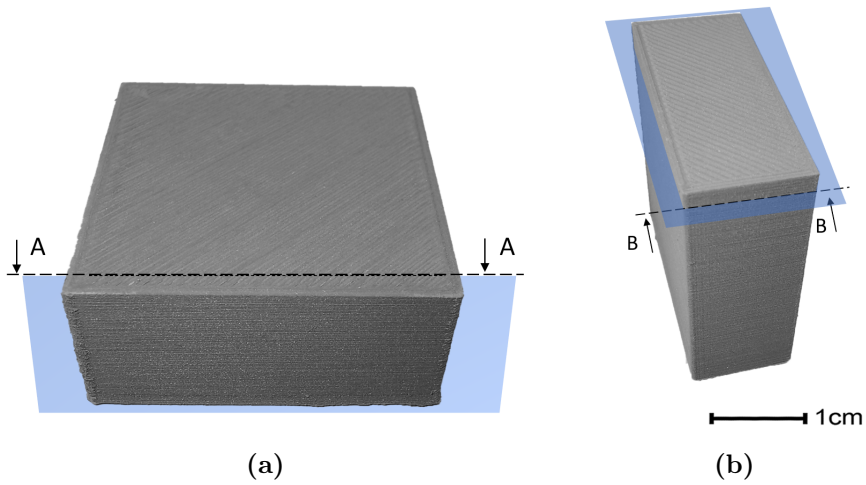


Figure 3.2.2: Schematic of both laying and standing Vickers specimen as presented in Figure 3.2.3.

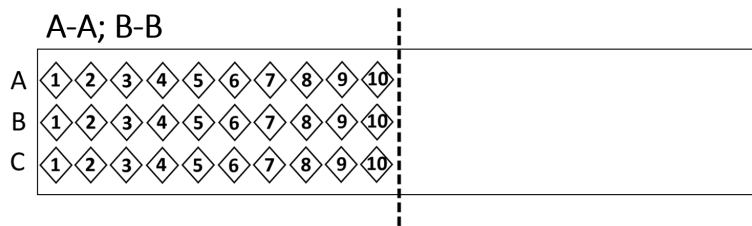


Figure 3.2.3: Points were the values were taken, equal for both Flat Top and Vertical Back specimens.

Apparatus

Microhardness testing was performed using the Mitutoyo HM-200 series microhardness tester (Mitutoyo Corporation, Japan) [59].

The microhardness tester was then used to apply a load to the surface of the specimen and measure the resulting indentation. The hardness was calculated using the indentation size and the load applied.

3.3 Tensile Tests

To perform the tensile test on metal 316L, dogbone-shaped specimens were machined from the cuboids. The dogbone shape allows for uniform stress distribution and reduced stress concentration during the test. The specimens were carefully prepared to meet the dimensional ratio requirements [51]. Prior to testing, the specimens were visually inspected to ensure they were free from defects or irregularities that could impact the test results.

The specimens were securely clamped in the testing machine using a fixture designed to prevent slippage and ensure proper alignment during the test. The fixtures were carefully selected to match the specimen dimensions and geometry, allowing for uniform loading and minimizing stress concentration effects. The alignment of the specimens within the fixtures was meticulously adjusted to ensure accurate force application during the test.



Figure 3.3.1: Image of fixture in [60].

Once the specimens were properly mounted, the tensile test was initiated. The loading rate, typically specified in the experimental plan, was applied uniformly until the specimens reached failure.

3.3.1 Apparatus

The tensile testing was conducted using the MTS Criterion Model 42 testing machine [60]. This machine, manufactured by MTS Systems Corporation, is widely recognized for its accuracy and reliability in conducting various mechanical tests. The Model 42 provides a maximum load capacity of 5 kN and a maximum displacement capability of 500 mm. The testing machine is equipped with a load cell that ensures precise measurement of the applied load. DIC [61] as mentioned later in section 3.4.2.1, was used for the painted specimens with a frequency acquisition of 5 Hz and a displacement rate of 1mm/min.

3.4 3-Point Bending Tests

3.4.1 Finite Element Simulations

For each of the notched geometries, the maximum stress at the apex of the notches was calculated. The stress concentrator factor Kt was also obtained. Finally, another model was analysed considering the case of ideal crack instead of a blunt notch. In this case the stress intensity factor $K1$ was obtained.

The first step in the simulation process was to create a 2D sketch of the specimen geometry, using Abaqus. The dimensions of the specimen were defined, as in subsection 3.1.2, and the notches were added to the sketch. The material model assigned was a linear elastic material [33] [62].

The second step is applying the boundary conditions, where the concentrated force of 1N and two displacement conditions were introduced. 1N is a "symbolic" value as the Kt has no dependency on the load applied. The two conditions simulate the two lower rollers of the fixture touching the 3-point bending specimens.

Finally, a suitable mesh is created on the model, as seen in Figure 4.7.3.

To determine the stress concentration factor (Kt) for the notched specimens, the following equation was used.

$$Kt = \frac{\sigma_{notch}}{\sigma_{nominal}} \quad (3.6)$$

where σ_{notch} is the maximum stress at the apex of the notch, and $\sigma_{nominal}$ is the stress in the specimen without the notch. An example can be found in chapter D. The value of the maximum nominal stress was obtained with another simulation on another 3BP specimen without a crack or a notch, with the same dimensions. The maximum stress was determined using a 1N load, and this value was used to calculate the stress concentration factor.

To calculate the stress intensity factor under Mode 1 Loading, K1 values for a specimen with a crack, another 2D sketch of the specimen geometry was created, and the dimensions of the specimen were defined. A crack was added to the specimen, and the K1 values were calculated using the finite element method. Based on the proportionality among K1 and the load applied on the simulation, it is possible to predict an estimate of the failure load if the specimens presented a crack.

Software

The simulations were conducted using ABAQUS software version X (Dassault Systèmes Simulia Corp., Providence, RI, USA) [63]. ABAQUS is a powerful and widely used finite element analysis software that is commonly employed in engineering applications. It provides a user-friendly interface and offers a broad range of features and capabilities to simulate various types of problems, including structural, thermal, and fluid dynamics analyses.

3.4.2 Tests Procedures

Two different methods were initially considered for conducting the tests: the compliance method and the basic procedure. The compliance method was selected as the initial approach, aiming to achieve precise and accurate results. However, due to unforeseen challenges in achieving a precrack in the specimens, the compliance method had to be replaced with a simplified version of the basic procedure.

3.4.2.1 Compliance Test

The compliance method, as outlined in the ASTM E1820-20 standard [52], is a widely used approach for measuring the fracture toughness of metallic materials. The procedure involves the use of a single-edge notch bend (SENB) specimen, which is typically machined from the material of interest. The specimen is subjected to a linearly increasing load until it yields. Afterward, the specimens are subjected to loading-unloading cycles until it fractures.

The compliance method determines the fracture toughness value through the analysis of the load-displacement curve. The load and displacement data is used to calculate compliance C , which represents the specimen's deformation response to a given load. The compliance C is then used to calculate the crack tip opening displacement (CTOD) and fracture toughness.

The data obtained from the compliance method can be used to calculate the fracture toughness value using various approaches, including the ASTM E1820-20 standard equations [52].

It is important to note that the compliance method has limitations and may not be suitable for all materials or specimen configurations, as proved in this case.

Painting Of Specimens

In order to use Digital Image Correlation (DIC) analysis [61], during compliance testing, the specimens were painted white and dots were added to provide the necessary contrast for DIC analysis. The painting process involved coating the specimens with a white spray paint, followed by the application of black dots using a fine-tip marker. The dots were spaced evenly along the length of the specimens to ensure accurate measurement of strain and deformation during testing. This painting technique allowed for precise measurement of the mechanical properties of the specimens and provided valuable data for analysis.

Apparatus

The experiment was conducted employing a StepLab - Axial 20 kN, mentioned in section 3.4.2.2.

Digital Image Correlation (DIC) software [61], is a widely used technique to analyze the deformation of materials under loading conditions. For this experiment, Vic-2D-v6 software (Correlated Solutions, Inc., USA) was employed to perform DIC analysis on the digital images of the specimens taken during the tensile test. Vic-2D-v6 is a user-friendly software that utilizes image correlation algorithms to track the displacement of the specimen's surface and calculate strain and other deformation parameters. The software provided a broad range of features and capabilities to perform DIC analysis, including strain maps, deformation plots, and stress-strain curves.

During the experiment, high-resolution images of the specimens were captured using a camera, and Vic-2D-v6 was used to process the images and obtain the deformation data. The software was also used to calculate strain rate, displacement, and other parameters to provide a comprehensive understanding of the deformation behavior of the specimens.

3.4.2.2 Basic Procedure

The ASTM E 1820 – 08a standard [52], provides a standardized method for measuring fracture toughness. The "basic procedure" is one of the methods described in this standard, and it involves conducting a test using a pre-cracked specimen. The test is performed at a constant rate of loading, and the force and displacement data are collected during the test. According to the standard, different types of specimens can be used. It was chosen to perform 3-point bending specimens, using therefore a single-edge notch geometry.

The data collected from the test can be used to calculate the fracture toughness of the material, which is a measure of the material's ability to resist the growth of cracks. To obtain the fracture toughness values, several parameters are needed, including the crack length, specimen geometry, and applied load. These parameters can be obtained from the data collected during the test.

The fracture toughness values obtained from this test method can be used to evaluate the performance of a material under different loading conditions and to compare the fracture toughness of different materials. This information is particularly useful in applications where the material is subjected to cyclic loading or where the material is expected to resist the growth of cracks.

Apparatus

The experiment was conducted using a StepLab - Axial 20 kN testing machine (Step Engineering S.r.l., Italy) [64]. This machine is capable of applying a tensile load of up to 20 kN with a maximum displacement of 500 mm. The machine was equipped with a load cell that provided accurate measurements of the applied load.

The specimens were clamped in the machine using custom-made fixtures that ensured proper alignment and prevented slippage during the test. The testing machine was controlled by a computer, which allowed for precise control of the loading rate and the data acquisition process.

3.5 Fractography

In order to examine the topographical features and morphology of the fracture surfaces, Scanning Electron Microscope (SEM) [65], imaging was performed. The following step-by-step procedure was implemented for the SEM analysis of the fracture surface.

Firstly, utmost care was taken during the sample preparation stage to maintain the integrity of the fracture surface. The specimens were delicately handled to avoid any damage or alteration to the fractured area. Additionally, any loose debris or extraneous particles present on the surface can meticulously eliminated using either gentle bursts of compressed air or a soft brush. In addition, an ultrasonic bath with acetone was performed.

Next, to facilitate the SEM analysis, the specimens were mounted onto SEM stubs. Attention was paid to establish good electrical contact between the specimen and the stub to minimize any potential charging effects during imaging.

Once the mounting was complete, the prepared specimens were transferred to the SEM chamber for imaging. The SEM instrument parameters, such as the accelerating voltage, beam current, and working distance, were carefully adjusted to optimize the imaging conditions.

Finally, the fracture surfaces were scanned using the SEM at various magnifications, allowing for a comprehensive analysis of the topography and morphology. The resulting SEM images provided valuable insights into the fracture mechanisms, crack propagation patterns, and surface characteristics of the specimens.

Apparatus

The Scanning Electron Microscope (SEM) used in this study was the FEI QUANTA 650 FEG SEM [65]. The FEI QUANTA 650 FEG SEM is a state-of-the-art instrument equipped with a field emission gun (FEG) as the electron source, allowing for high-resolution imaging and excellent electron beam stability.

SEM imaging was employed to investigate the microstructural characteristics and surface morphology of the specimens. The FEI QUANTA 650 FEG SEM offers a wide range of magnification options, providing the ability to examine materials at various scales, from macro- to nanoscale. This capability facilitated the detailed analysis of microstructural features, surface defects, and fracture surfaces of the specimens.

The FEI QUANTA 650 FEG SEM was utilized to capture high-resolution images of the specimens at different magnifications. These images can subsequently be analyzed to gain insights into the microstructural properties, such as grain morphology, phase distribution, and surface features.

RESULTS

The results of the present work are presented in the following sections.

4.1 Specimen Preparation

The initial step in the experimental phase of the thesis involved the meticulous extraction of specimens to be subjected to both tensile and three-point bending tests, employing the utilization of an EDM (Electrical Discharge Machining) machine [50]. This precision extraction process ensured the acquisition of high-quality samples for subsequent mechanical testing and analysis. The specimens underwent thorough preparation procedures after cutting, including grinding, polishing, and painting, which resulted in refined surfaces.

Extraction Of Dogbone Specimens



Figure 4.1.1: Cutting of Dogbone specimens.



Figure 4.1.2: Dogbone specimen after cutting and painting.


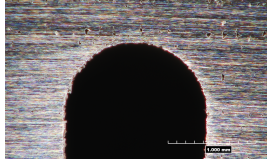
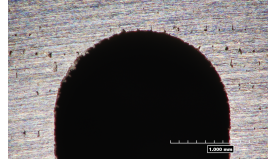
Extraction Of 3-Point Bending Specimens



Figure 4.1.3: Cutting Of 3-Point Bending Specimens.

The Flat Front, Flat Back, Vertical Front and Vertical Back specimens are identical.

Table 4.1.1: Notch size on specimens taken from Vertical Front for illustrative proposes, scale bar: 1 mm.

Blue	Yellow	Green
		
0.52 mm	1.62 mm	2.01 mm

4.2 Particle Size Measurement

As highlighted in Chapter 2, the theoretical section, the characteristics of the filament play a crucial role in influencing the outcomes of the MEAM process. In the context of this study, a commercial filament was employed. It was deemed valuable to examine the cross sections and measure the particle size.

Consequently, the filament embedded within the resin was extracted from the mold, subjected to gentle grinding, and observed under a microscope as presented below.

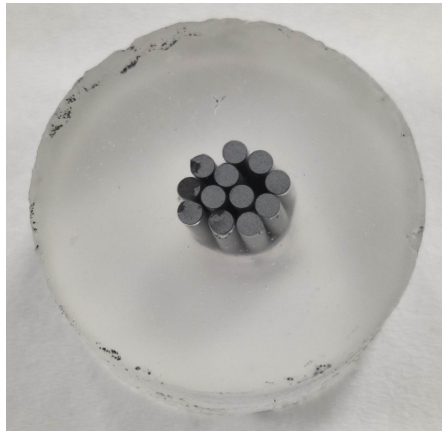
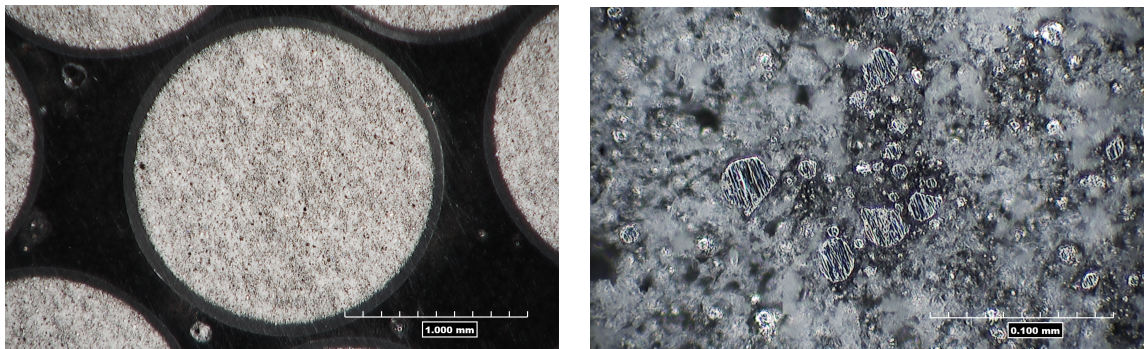


Figure 4.2.1: Embedded filament.

The filament has a diameter of **1.75 mm**, other diameters are available on the marked, such as **2.85 mm** [49]. A close-up of the filament strings embedded is shown below.



(a) Close-up on middle filament string on the embedded shell, scale 1 mm.

(b) Visual representation of particles on the filament, scale 0.1 mm.

Figure 4.2.2

Both Top and Bottom Side of the embedding are still the same filament and should therefore have the same values. The particle measurements can be found in chapter A on the Appendix, giving an average value of **16 micrometers**.

4.3 Surface Roughness Evaluation

The total values for each roughness test can be found in chapter B in the Appendix. 3D images and plots gotten from Hirox [53] can also be found there. A visual representation of these values is plotted below.

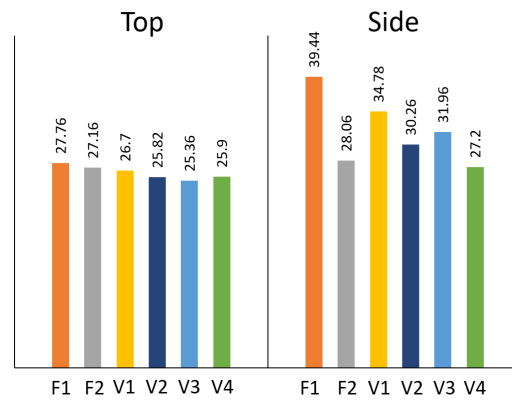


Figure 4.3.1: Bar plot of average roughness R_a in μm on the two surfaces tested for each cuboid, the detailed values for the averages can be found in chapter B.

Cuboid surface representation is shown in figure 4.3.2.

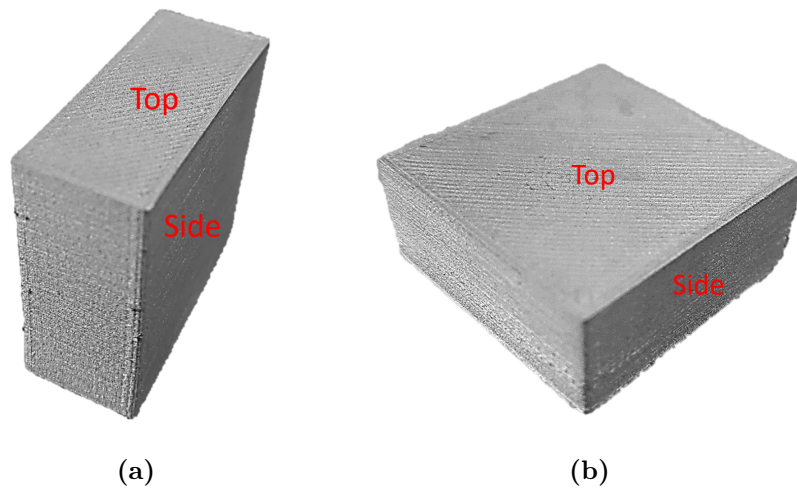


Figure 4.3.2: Surface tested on the cuboids.

4.4 Defects and Porosity Distribution

The evaluation was performed on two specimen types: flat and vertical. Figure 4.4.1 presents the representation of defects and porosity distribution on the flat specimens.

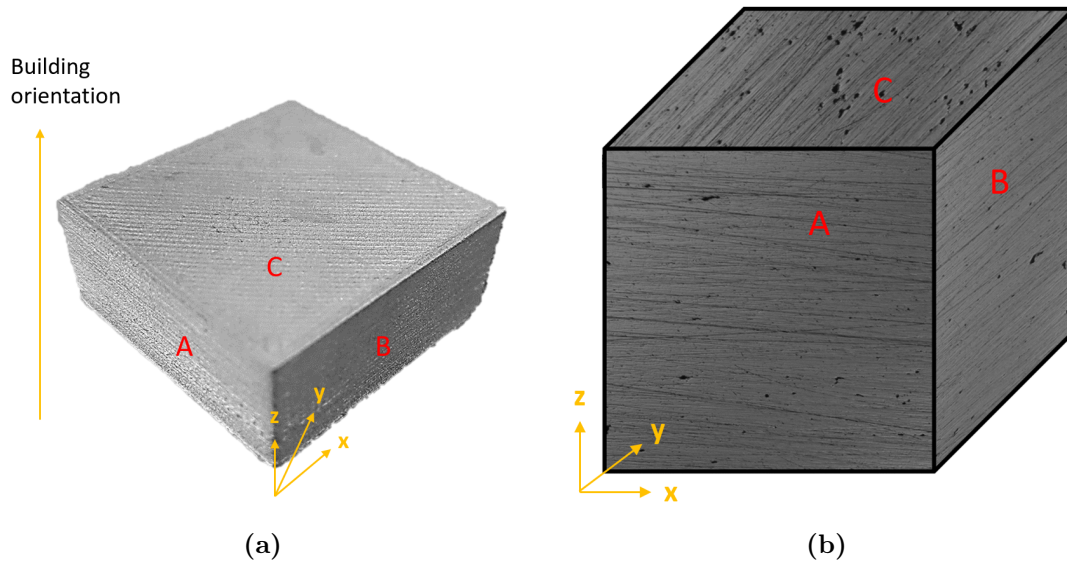


Figure 4.4.1: Defects and porosity distribution representation on flat specimens.

Figure 4.4.2 showcases the defects and porosity distribution on the vertical specimens.

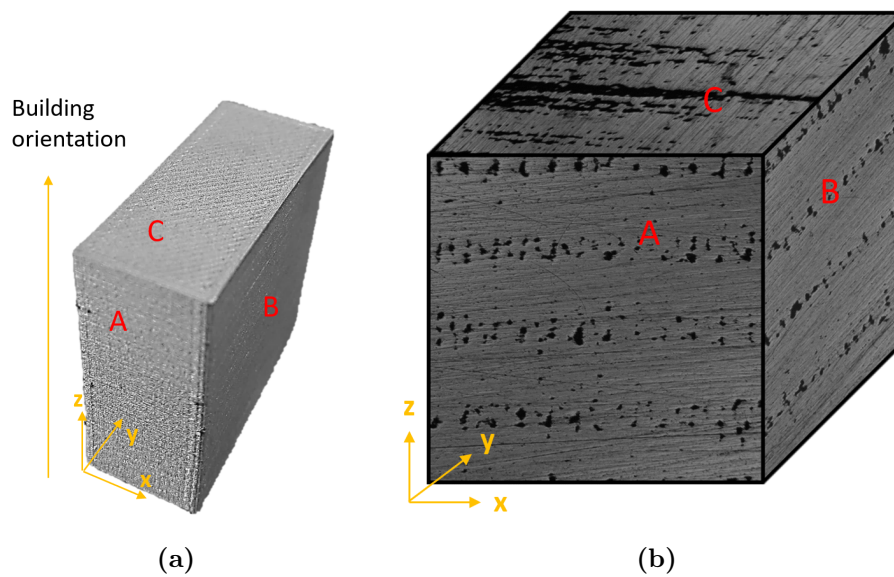


Figure 4.4.2: Defects and porosity distribution representation on vertical specimens.

4.5 Grain Size Measurement

The grain size of the printed specimens was measured as described in Chapter 6. Two types of specimens were analyzed: flat top and vertical back. The grain size measurement technique is based on the standard E112-10 [56].

Flat Top

Figure 4.5.1 shows the microstructure of the flat top specimens after etching, with a scale of 100 μm and a magnification of 20 μm . It yielded a value of 38.7 μm .

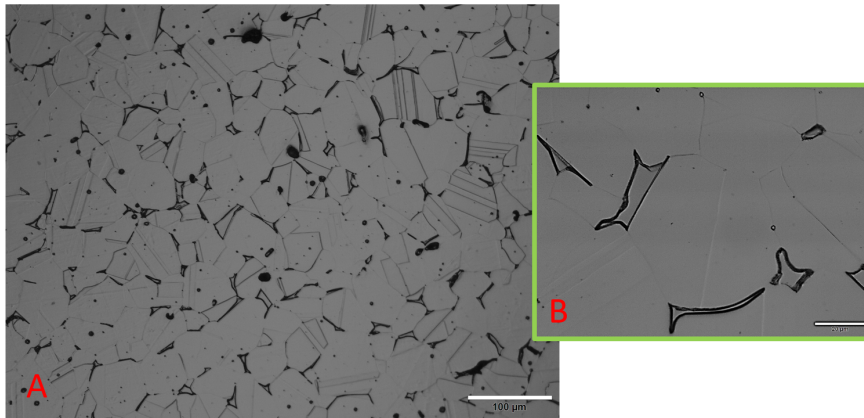


Figure 4.5.1: A) 100 μm scale and B) magnification in 20 μm .

Vertical Back

The microstructure of the vertical back specimens after etching is depicted in Figure 4.5.2, with a scale of 100 μm and a magnification of 20 μm . The measured average grain size is 37.2 μm .

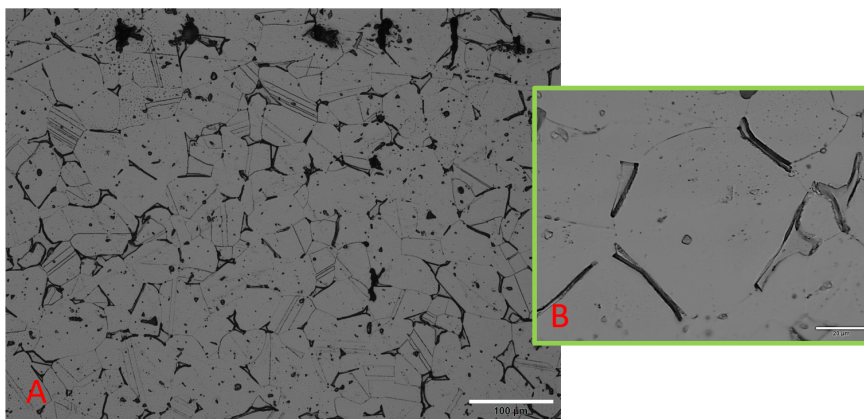


Figure 4.5.2: A) 100 μm scale and B) magnification in 20 μm .

4.6 Microhardness - Vickers

The reference standard [66] was used as the guideline for the testing procedure. Points for microhardness testing were selected as shown in figure 4.6.1, in regards to Figure 3.2.3, as shown below.

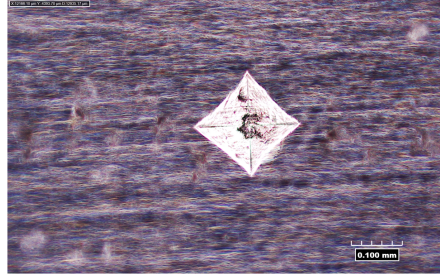


Figure 4.6.1: Vickers microhardness dentation example, scale 0.1 *mm*.

Flat Top:

Table 4.6.1 presents the average microhardness values (H2.0) for the flat top specimens. The measurements were performed at multiple points, and the results for each point can be found in table C.0.1 in the Appendix.

Table 4.6.1: H2.0 Average Values on Flat Top specimens, measured in micrometers.

<i>Average A:</i>	104.71
<i>Average B:</i>	111.16
<i>Average C:</i>	110.62

Vertical Back:

The average microhardness values (H2.0) for the vertical back specimen are presented in table 4.6.2. The individual measurements for each point can be found in table C.0.2 in the Appendix.

Table 4.6.2: H2.0 Average Values on Vertical Back Specimen, measured in micrometers.

<i>Average A:</i>	97.17
<i>Average B:</i>	98.36
<i>Average C:</i>	98.94

Values for each point taken can be found in Table C.0.2 in the Appendix.

To visualize the microhardness data for both specimen types, figure 4.6.2 shows a plot representing the microhardness values obtained. The plot provides a comparative analysis of the microhardness between the flat top and vertical back specimens.

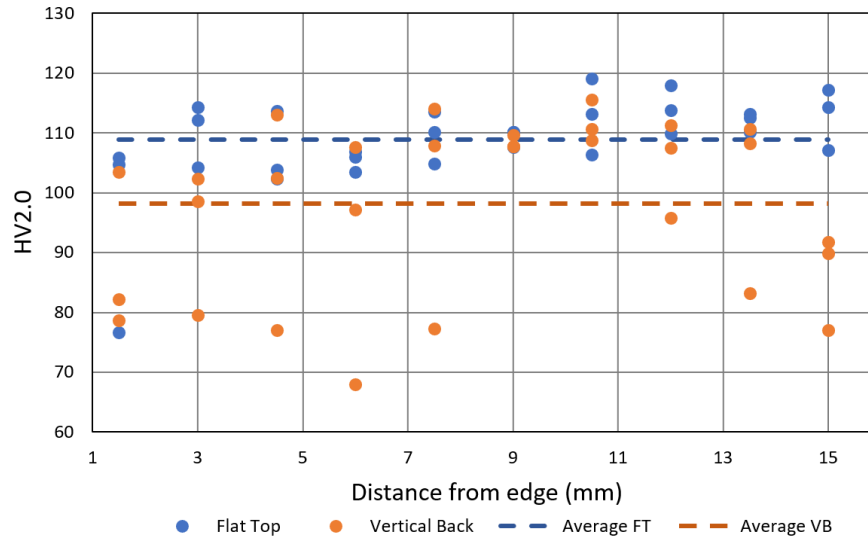


Figure 4.6.2: Microhardness data of both specimens.

4.7 Finite Element Simulations

The 3-point bending tests were simulated using a CAE software, according to subsection 3.4.1. The following 5 simulations were performed:

- One simulation for each of the three notch geometries presented in subsection 3.1.2.1.
- One simulation for a fictual *perfect* crack.
- one with neither notch or crack.

The following is a simulation for the case of subsection 3.1.2.1, here representative for all simulations.

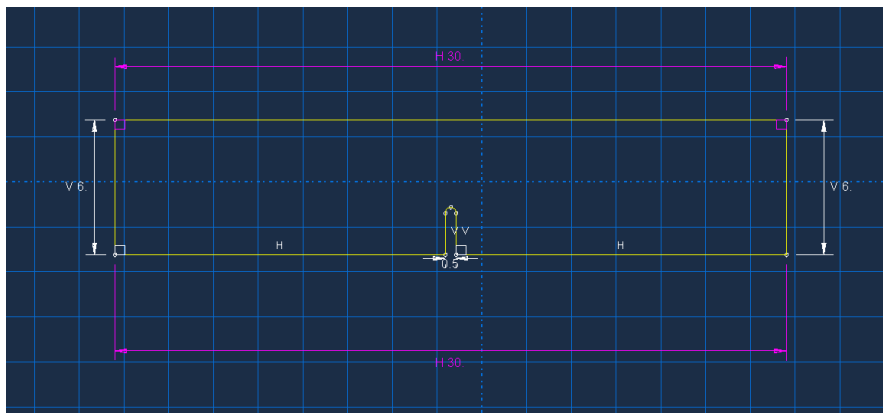


Figure 4.7.1: Sketch of simulation.

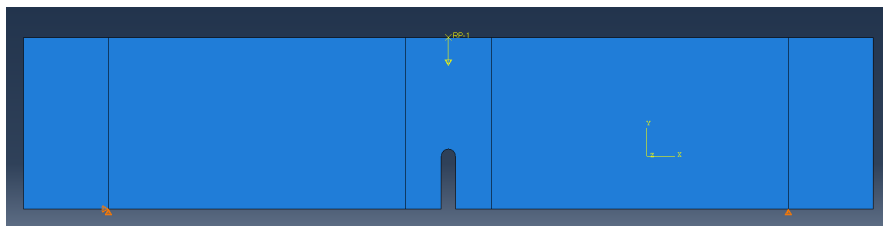


Figure 4.7.2: Boundary condition and loading applied.

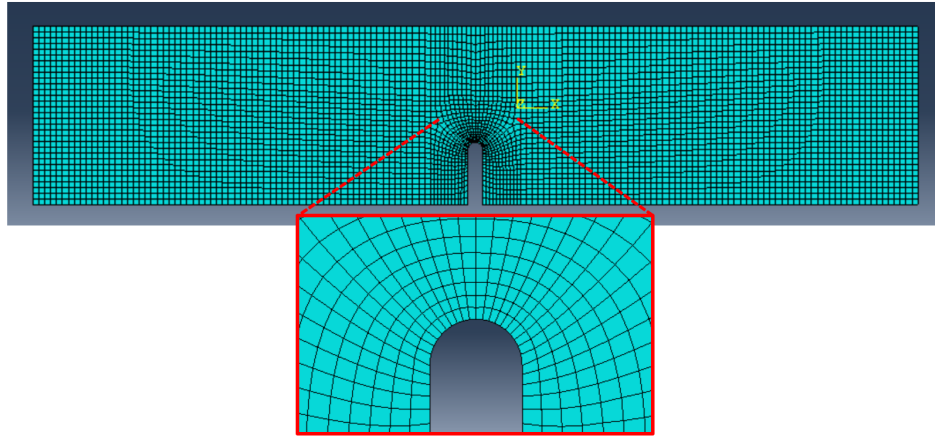


Figure 4.7.3: Mesh on simulation.

Table 4.7.1 presents the calculated K_t values for the representative simulation. The K_t values provide insights into the stress distribution and indicate the level of stress concentration at the notches or cracks. An example of the calculation of K_t can be found in chapter D.

Table 4.7.1: K_t values from simulations in $\text{MPa}\sqrt{\text{mm}}$.

<i>Simulation</i>	σ_{notch}	<i>K_t</i>
"Perfect" crack	0.93830	
1	2.29909	7.21745
2	1.57397	4.94110
3	1.38010	4.33250
No Notch/Crack	0.31855	2.94557

4.8 Tensile Test

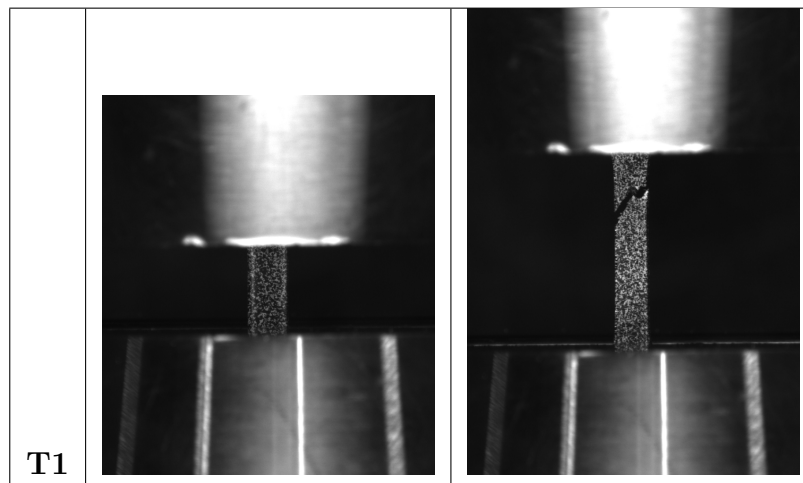
The tensile tests were performed using the MTS Criterion Electromechanical Load Frame (MTS Systems Corporation) [67], with a Load - Displacement of 1 mm/min. Table 4.8.1 presents the different tensile specimens used in the study and their respective printed orientation.

Table 4.8.1: Tensile specimens with their respective printed orientation.

<i>Specimen</i>	<i>Cuboid</i>
T1	Vertical
T2	Vertical
T3	Flat
T4	Flat

Table 4.8.2 shows an illustration on the crack for specimen T1.

Table 4.8.2: DIC before/after fracture images of T1 for illustrative purposes.



A stress-strain plot for the specimens tested is presented in Figure 4.8.1.

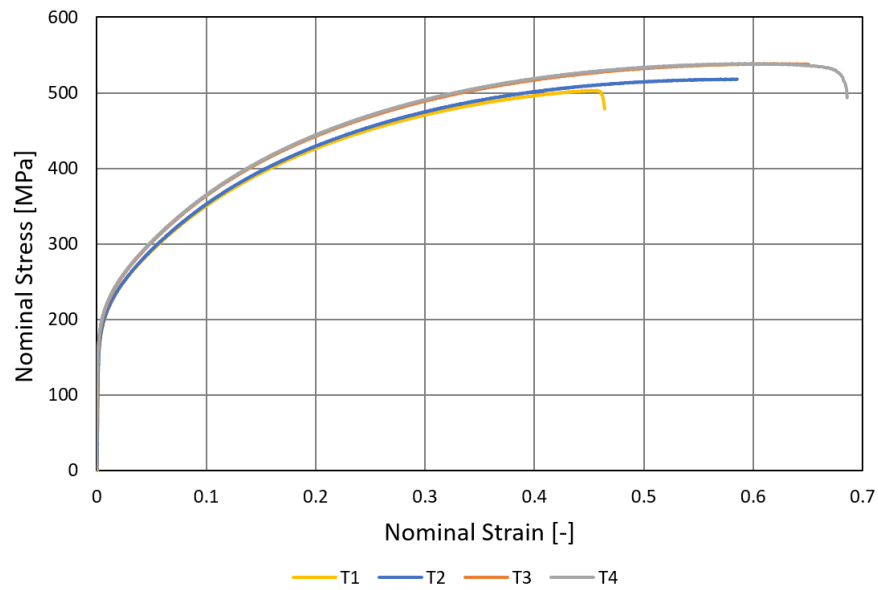


Figure 4.8.1: Stress-Strain plot for the specimens tested with Tensile test.

The table below presents the maximum stress the specimens could withstand before fracture.

Table 4.8.3: Ultimate Tensile Strength for each specimen.

	<i>Stress</i>	<i>Strain</i>
T1	0.452262	503.1944
T2	0.585033	518.1524
T3	0.600057	538.5281
T4	0.609975	538.6945

4.9 Fracture Tests

4.9.1 Compliance Test

Despite the initial focus on the compliance method, multiple attempts were made to utilize this approach to obtain meaningful data. However, these attempts proved to be unsuccessful in obtaining the desired results due to two main challenges. Firstly, the precracking process posed a significant difficulty, primarily because the material under investigation exhibited a high level of ductility, as also evident from the tensile tests. The inherent ductility of the material made it challenging to initiate and propagate a controlled crack. Several techniques were explored to overcome this issue, including adjusting the loading conditions and implementing specialized notch geometry. However, the desired crack control and reproducibility level could not be achieved. Secondly, the size of the specimens posed another significant obstacle. The specimens used in the compliance tests were too small relative to the fixture, making it impossible to attach conventional extensometers for direct strain measurements. Digital Image Correlation (DIC) was employed as a potential alternative to recording crack mouth opening displacement. Unfortunately, due to the limitations of the DIC system and the complex nature of crack propagation, the measurements obtained were imprecise and unreliable. The inherent difficulties associated with accurately capturing the crack mouth opening displacement hindered the effectiveness of the compliance method in obtaining precise and consistent results.

Nevertheless, despite these challenges, valuable insights were gained from these unsuccessful attempts. The difficulties encountered during the precracking process and the limitations of extensometer usage highlighted the need for alternative methodologies and further exploration. These insights and lessons learned are further discussed in detail in the subsequent chapters, paving the way for potential future improvements and advancements.

4.9.2 Basic Procedure

The fracture test was performed on two types of specimens: flat and vertical. Figure 4.9.1 shows the fracture behavior of the flat specimens, while figure 4.9.2 illustrates the fracture behavior of the vertical specimens.

The fracture tests were also conducted with different notch sizes. Figures 4.9.3, 4.9.4, and 4.9.5 represent the fracture behavior of specimens with stress ratios of R0.25, R0.50, and R1.00, respectively.

Table 4.9.1 and Table 4.9.2 present specific values of the data used for the plots.

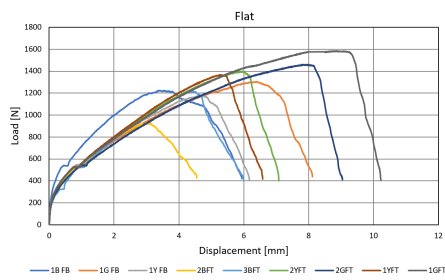


Figure 4.9.1: Flat specimens.

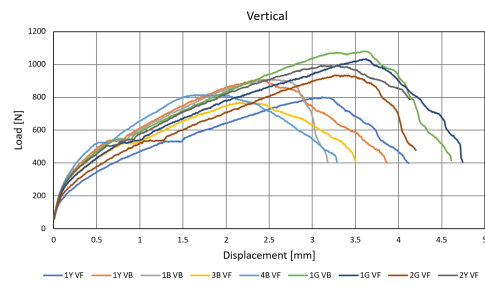


Figure 4.9.2: Vertical specimens.

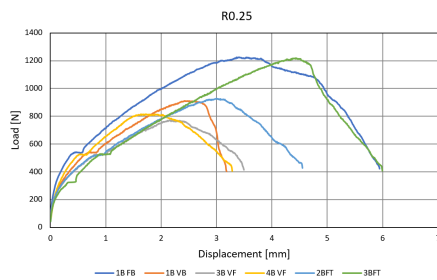


Figure 4.9.3: R0.25

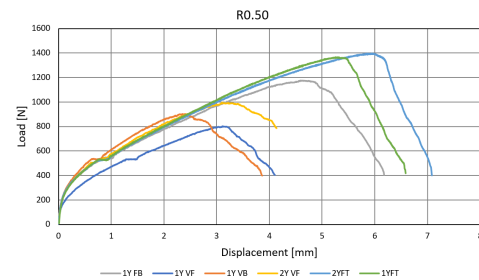


Figure 4.9.4: R0.50

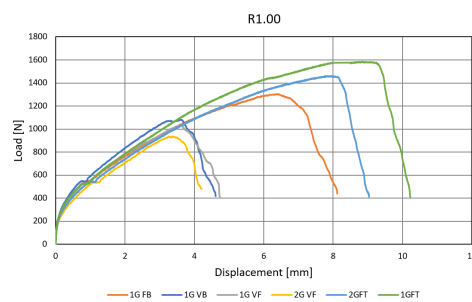


Figure 4.9.5: R1.00

Table 4.9.1: Load values of the basic procedure curves.

	<i>Average Load at Plateau [N]</i>	<i>Maximum Load [N]</i>
1YVF	530	801.65
1GVF	520	1033.25
2YVF	540	987.15
2GVF	530	934.45
3BVF	550	769.99
4BVF	520	814.86
1YVB	530	902.85
1BVB	540	909.27
1GVB	545	1081.67
1YFT	530	1366.12
1GFT	520	1584.39
2BFT	515	928.12
2YFT	520	1399.11
2GFT	540	1461.34
3BFT	520	1217.55
1BFB	540	1223.61
1YFB	550	1176.39
1GFB	550	1302.87

The fracture tests conducted here were static fracture tests. It is important to note that the fracture toughness values obtained from these tests are merely indicative due to certain deviations from the standard protocol [52]. Specifically, the specimens were not pre-cracked as outlined in the basic procedure. The measurement of crack propagation was not feasible due to a lack of available equipment. The indicative average values of the fracture toughness, for each notch size are presented below.

Table 4.9.2: Average indicative fracture toughness values for each notch size.

	<i>Vertical</i>			<i>Flat</i>		
	R=0.25	R=0.5	R=1.0	R=0.25	R=0.5	R=1.0
<i>Fracture Toughness [MPam]</i>	39.0	42.1	47.7	52.7	61.6	68.0

4.10 Fractography

4.10.1 Dogbone Fractured Surface

Table 4.10.1, table 4.10.2, table 4.10.3, and table 4.10.4 present a visual representation of the specimens T1, T2, T3, and T4, respectively, showing their appearance before and after the tensile test presented in section 4.8. These tables provide comparative images that highlight the changes in the specimens' fracture surfaces due to the applied stress during the test.

Table 4.10.1: Before and after visual representation of specimen T1, scale 1.000 mm.

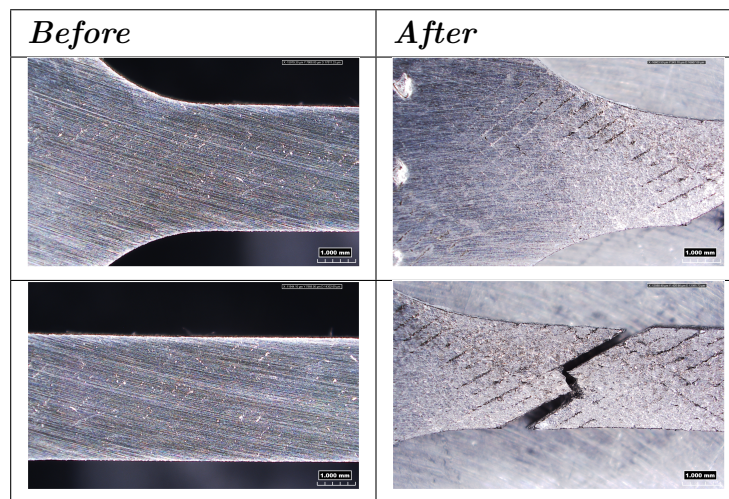


Table 4.10.2: Before and after visual representation of specimen T2, scale 1.000 mm.

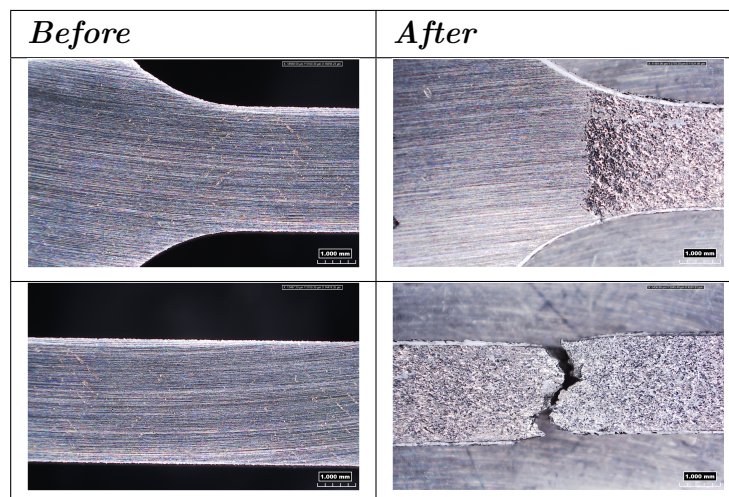


Table 4.10.3: Before and after visual representation of specimen T3, scale 1.000 mm.

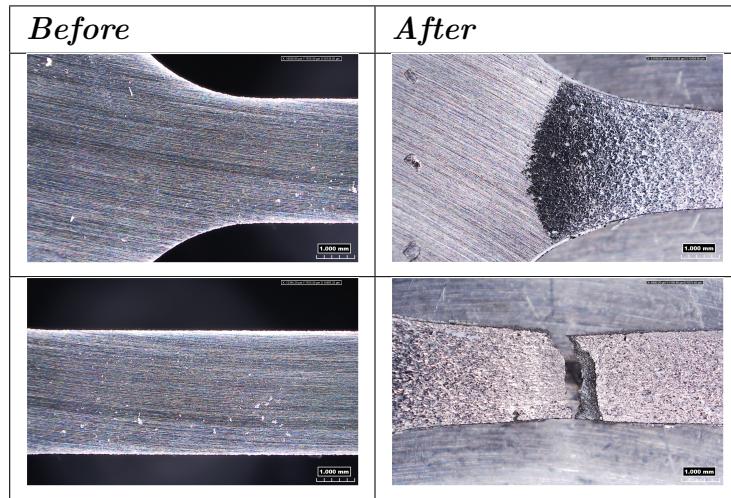
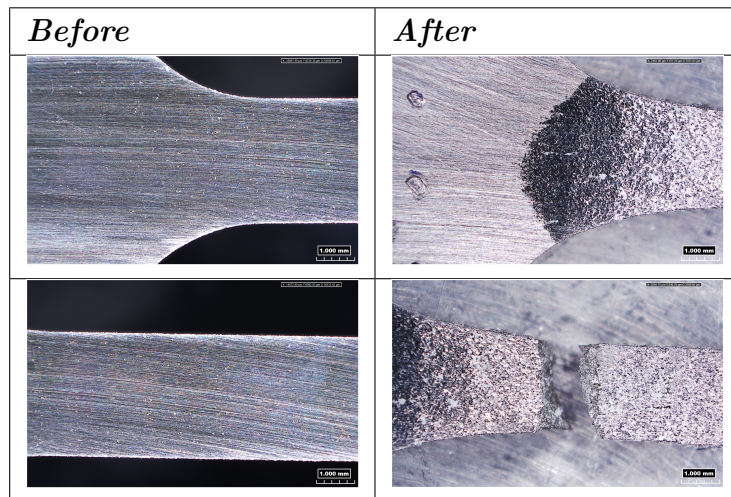


Table 4.10.4: Before and after visual representation of specimen T4, scale 1.000 mm.



4.10.2 Etching on 3-Point Bending Fractured Surface

Vertical Front

Figure 4.10.1 shows the etched crack on the vertical front of the fractured surface. The magnified view of the etched crack is presented in Figure 4.10.2, providing a closer look at the crack's characteristics.

Figure 4.10.3 presents a magnified view of the etched surface surrounding the crack.

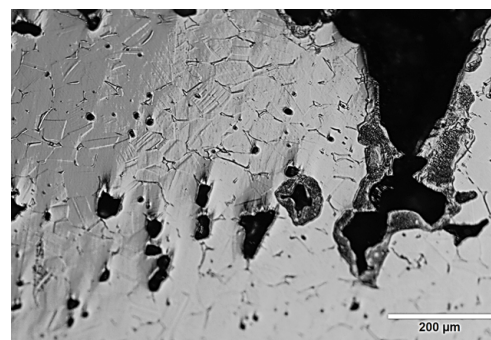
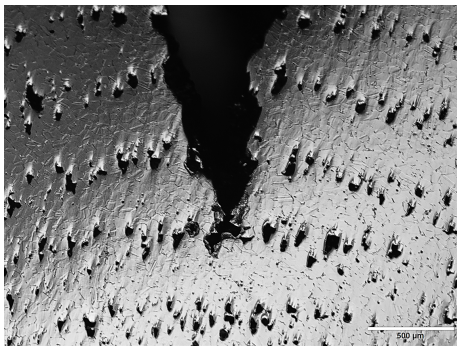


Figure 4.10.1: Etched crack, scale 500 μm. **Figure 4.10.2:** Magnified etched crack, scale 200 μm.

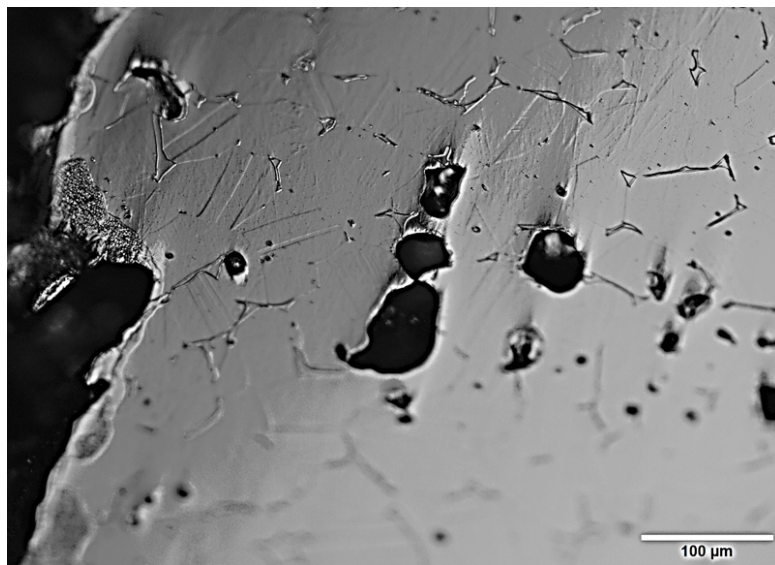


Figure 4.10.3: Magnified etched surface, scale 100 μm.

4.10.3 SEM of 3-Point Bending Fractured Surface

Table 4.10.5 shows the SEM images captured on the vertical front specimens. The table presents the SEM image of specimen 1YVF and provides a closer view of a specific region of interest. The SEM image of specimen 4BVF, and the magnified view of the selected area.

Table 4.10.5: SEM on Vertical Front Specimens.

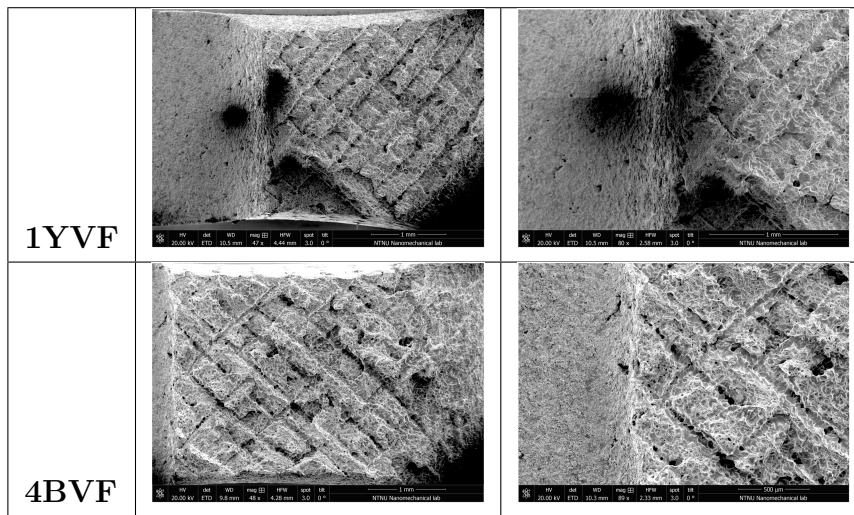


Table 4.10.6 displays the SEM images obtained from the vertical back specimens. The table presents the SEM image of specimen 1GVB, and zooms in on a particular area of interest. The SEM image of specimen 1YVB, and provides a closer view of a selected region.

Table 4.10.6: SEM on Vertical Back Specimens.

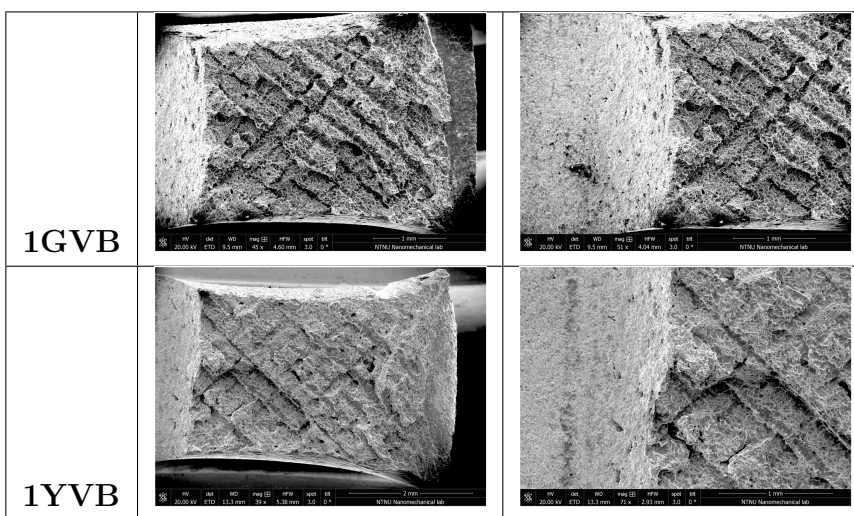


Table 4.10.7 presents the SEM image captured on the flat front specimen. The table showcases the SEM image of specimen 2BFT and provides an enlarged view of a specific area of interest.

Table 4.10.7: SEM on Flat Front Specimen.

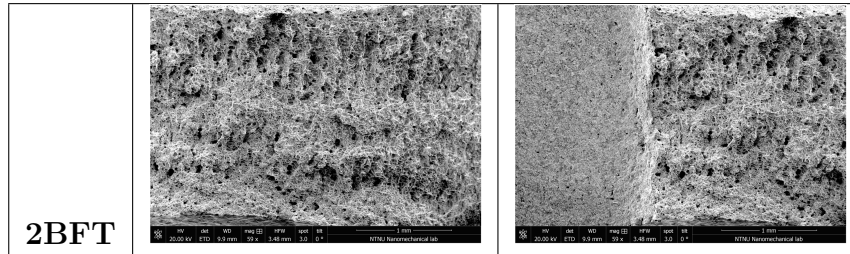
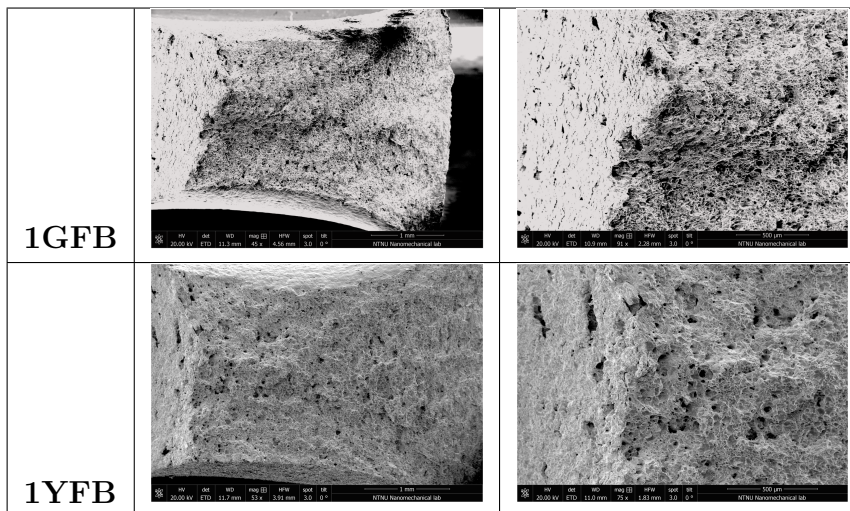


Table 4.10.8 exhibits the SEM images obtained from the flat back specimens. The table displays the SEM image of specimen 1GFB, and offers a magnified view of a selected region. It also shows the SEM image of specimen 1YFB, and presents a closer view of a particular area.

Table 4.10.8: SEM on Flat Back Specimens.



DISCUSSIONS

5.1 Specimen Preparation

Dogbone Specimens

The extraction process of dogbone specimens for tensile testing was conducted with precision and attention to detail. All necessary measures were taken to ensure the accuracy of the specimens. The dimensions of the specimens were carefully checked, and overall, the extraction process was successful. However, it was observed that in a few instances, the thickness of the specimens deviated by 0.01 from the intended dimensions. While this discrepancy is noteworthy, it is deemed to be within an acceptable range that should not significantly impact the test results. Despite this minor deviation, the extracted dogbone specimens are expected to yield reliable and representative data for the subsequent mechanical tests.

3-Point Bending Specimens

In contrast to the extraction of dogbone specimens, the process of extracting 3-point bending specimens encountered several challenges. Cutting the specimens proved to be a more complex task, resulting in a higher rate of failure. The notch sizes of the specimens were found to be less than ideal, with variations and imperfections observed. Consequently, in a few cases, it became necessary to replace some specimens due to the discrepancies in their notch sizes. These challenges primarily arose from inexperience and issues with the machine's cutting code. Although efforts were made to mitigate these difficulties, the imperfect notch sizes could introduce uncertainties and potentially impact the mechanical properties determined through 3-point bending tests.

5.2 Particle Size Measurements

The analysis yielded an average particle size of approximately 16 micrometers. It is possible that smaller particles, which were still within the microscope's range of focus, contributed to the observed average. Conversely, larger particles located further away from the focal plane might not have been captured by the measurements.

Furthermore, it is worth mentioning that a considerable amount of variation was observed in the particle sizes. This variation could arise from multiple factors, such as inconsistencies in the manufacturing process of the filament or inherent material properties. The wide range of particle sizes indicates that the filament utilized in the MEAM process contains particles of various dimensions, potentially influencing the mechanical properties and performance of the printed parts.

In relation to the homogeneity of the powder distribution within the filament, it is important to assess the impact of such variations on the final printed parts. Smaller particles may contribute to improved densification and sintering, leading to enhanced mechanical strength, while larger particles may introduce defects or porosity within the material matrix.

5.3 Surface Roughness Evaluation

The surface roughness evaluation was conducted on two surfaces of each tested cuboid. The results revealed interesting observations regarding the variation in surface roughness between different orientations of the cuboids. Specifically, it was noted that the Top surface, illustrated as the **A** in section 4.4, exhibited more consistent results, irrespective of the two different printed orientations, both flat and vertical. Conversely, the Side surface exhibited greater variation in surface roughness measurements. For the cuboids printed in a flat orientation, there was an average variation of approximately 10 micrometers in average roughness. On the other hand, for the cuboids printed in a vertical orientation, there was more variation than the Top but less than the flat-printed cuboids.

The consistent results observed on the Top surface, regardless of the printed orientation, may be attributed to several factors. Firstly, the Top surface experienced the same printing conditions and material deposition patterns, leading to uniform surface morphology. Additionally, the Top surface might have been less susceptible to certain printing-related artifacts, such as layer shifting or misalignment, which can contribute to increased surface roughness. The relative stability in the surface roughness measurements on the Top surface suggests that the printing process

and environmental conditions had a more consistent influence on this particular surface.

In contrast, the Side surface exhibited greater variation in surface roughness measurements. This variation may be influenced by factors such as the layering process and the specific geometry of the printed object. The layering process introduces the formation of individual layers, and any inconsistencies or imperfections in the layer deposition can contribute to variations in surface roughness. Additionally, the Side surface may be more susceptible to print defects, including uneven cooling, poor adhesion between layers, or inadequate support structures, which can affect the surface quality and result in increased roughness variation.

Considering the different orientations of the cuboids, it is expected that the flat-printed cuboids would exhibit a higher degree of surface roughness variation compared to the vertical-printed cuboids. The flat-printed cuboids have larger surface areas in contact with the build platform, leading to increased sensitivity to factors such as leveling, adhesion, and temperature gradients. These factors can introduce variations in the layering process and result in increased surface roughness variation. On the other hand, the vertical-printed cuboids experience a more consistent layering process, with smaller surface areas in contact with the build platform. This reduced contact area and more controlled layering process can contribute to relatively lower surface roughness variations compared to the flat-printed cuboids.

5.4 Defects and Porosity Distribution

The flat-printed specimen, representing the horizontal orientation, exhibits an overall lower density of pores compared to the vertical-printed specimen. This implies that the printing orientation plays a significant role in the formation and distribution of pores within the material.

Upon closer examination of the flat-printed specimen Figure 4.4.1, it is noteworthy that there is a slightly higher concentration of pores on the C surface, which corresponds to the top surface of the cube. This localized increase in porosity suggests that the printing and sintering process may have encountered challenges in achieving uniform material deposition and consolidation on this particular surface. This is the surface that corresponds to a layer, these pores are on the layer, not between layers. The presence of pores on the C surface may be attributed to factors such as insufficient material flow, inadequate bonding between layers, or variations in temperature and cooling rates during printing.

The vertical-printed specimen Figure 4.4.2, on the other hand, exhibits a more intriguing pattern of porosity distribution. The A and B surfaces, which represent

the side surfaces of the cube, display an identical pattern of pores arranged in horizontal lines. This characteristic distribution suggests that the printing process, specifically in the vertical direction, influenced the formation of these horizontal lines of porosity. It is likely that the material deposition and consolidation in the vertical direction resulted in the development of these distinctive pore lines.

Additionally, it is important to address the presence of deep lines on the C surface (top) of the vertical cube, which may resemble pores but are more likely related to factors encountered during the printing phase. These deep lines could be attributed to irregularities in material flow, variations in printing parameters subsection 2.1.4, or mechanical disturbances during the build process.

5.5 Grain Size Measurement

For the flat specimen, as depicted in section 4.5, a grain size measurement was performed according to the standard E112-10 [56]. The average grain size value obtained from the analysis was determined to be approximately 38.7 μm . This value signifies the average diameter of the grains present in the material's microstructure. A larger grain size typically indicates a coarser microstructure, which can impact the material's mechanical properties.

Similarly, for the vertical specimen, as shown in section 4.5, the grain size measurement yielded an average value of approximately 37.2 μm . This measurement suggests a microstructure with a similar average grain diameter as the flat specimen. However, it is crucial to interpret these grain size measurements within the context of the material's fabrication process, including the 3D printing and sintering steps.

The observed average grain sizes of approximately 38.7 μm for the flat specimen and 37.2 μm for the vertical specimen suggest a microstructure with moderately sized grains. Larger grain sizes may lead to reduced strength but increased ductility, while smaller grain sizes can enhance strength at the expense of ductility.

5.6 Microhardness - Vickers

Upon analyzing the microhardness results, it is evident that the values near or on pores exhibited noticeably lower microhardness values, typically below 100. This observation suggests that the pores might have influenced the material's hardness properties, leading to decreased values in the affected regions. The pores can result from excess material being deposited during the 3D printing process, potentially altering the microstructure and introducing variations in hardness. These lower microhardness values near the pores could indicate a change in material properties due to differences in grain structure.

For the flat top specimens, the average HV2.0 microhardness values were determined as 104.71, 111.16, and 110.62, respectively, as shown in Table 4.6.1. The points taken for analysis are illustrated in Figure 4.6.2. These values indicate a certain level of hardness in the material, with some slight variations among different measurement points. It is worth noting that the average microhardness value for the flat specimen HV2.0 was approximately 10 units higher than the average for the vertical back specimen, indicating a potential difference in hardness between the two orientations.

In the case of the vertical back specimens, the average HV2.0 microhardness values were found to be 97.17, 98.36, and 98.94, as presented in Table 4.6.2. The points considered for analysis can be seen in Figure 4.6.2. Factors such as layering patterns, cooling rates, and the influence of gravity can affect the material's microstructure and subsequent hardness properties.

5.7 Finite Element Simulations

To evaluate the effect of different notches and cracks on the stress concentration in the material, simulations were conducted to calculate the stress intensity factor (Kt) values. The values obtained from the simulations are presented in Table 4.7.1.

From the results, it is observed that the "Perfect" crack simulation yielded the σ value of 0.93830. This indicates a relatively high-stress concentration at the crack. Simulation 1, which corresponds to subsection 3.1.2.1, resulted in a stress intensity factor (Kt) value of 7.21745. This value suggests a substantial stress concentration at the notch, indicating that the chosen notch geometry has a considerable impact on the stress distribution and potential failure modes.

Simulation 2, representing subsection 3.1.2.2, yielded a Kt value of 4.94110. Although lower than in Simulation 1, this value still indicates the presence of

stress concentration at the notch, emphasizing the influence of notch geometry on the material's stress distribution.

Simulation 3, associated with subsection 3.1.2.3, resulted in a K_t value of 4.33250. This value suggests a slightly lower stress concentration at the notch compared to Simulation 2, further highlighting the influence of notch geometry on the material's stress distribution and failure behavior.

In contrast, the simulation without any notch or crack (No Notch/Crack) exhibited a significantly lower K_t value of 2.94557. This indicates a reduced stress concentration in the absence of any geometrical irregularities, resulting in a more uniform stress distribution throughout the material.

Based on the higher K_t values observed for simulations with notches or cracks, it can be inferred that these regions are susceptible to failure initiation and propagation.

5.8 Tensile Tests

Four specimens were tested, with two specimens (T1 and T2) obtained from the vertically printed cuboid, and the other two specimens (T3 and T4) obtained from the flat printed cuboids.

It is observed that the elastic parts of the stress-strain curves for all specimens are similar, indicating a consistent elastic response, see Figure 4.8.1. This suggests that the sintering process and microstructure of 316L have resulted in similar elastic properties across the specimens. However, significant differences are observed in the fracture behavior and ultimate tensile strength.

T1 fractures at a nominal strain above 0.45, with a lower stress value of approximately 500 MPa. This indicates that T1 has lower strength compared to the other specimens. T2 fractures just below a nominal strain of 0.6, exhibiting a higher stress value than T1 but still lower than T3 and T4. T3 fractures at around 0.65 strain with a stress level of almost 550 MPa, while T4 exhibits a similar fracture strain but with a slightly higher strain value, still below 0.7. Both T3 and T4 show higher strength compared to T1 and T2.

These variations in fracture behavior and ultimate tensile strength can be attributed to several factors related to the sintering process and microstructure of 316L. The specimens are ductile, which aligns with the fracture behavior observed in the tested specimens. The high ductility of the material leads to premature yielding and reduced ultimate tensile strength compared to annealed AISI 316L. The reduction in elastic modulus observed in the sintered 316L material, 120 ± 17 GPa compared to the typical value of 193 GPa, can be attributed to the high

ductility. This suggests that the material yields at lower stress levels. The offset yield strength of 142 ± 10 MPa further confirms the premature yielding behavior. The ultimate tensile strength of 432 ± 17 MPa is lower than the typical value of 515 MPa for annealed AISI 316L, indicating reduced load-bearing capacity.

The high ductility and the absence of significant local necking observed in the tested specimens indicate a uniform elongation of the gauge during loading. This behavior is further supported by the total elongation at fracture, which exceeds the typical value, confirming the high ductility of the sintered material.

The maximum stress the specimens could withstand before fracture is presented in Table 4.8.3. T1 exhibited a maximum stress of approximately 500 MPa, while T2 showed a slightly higher value of about 518 MPa. On the other hand, T3 and T4 displayed significantly higher maximum stresses of approximately 539 MPa.

From Figure 2.1.2, it is evident that the specimens, directly printed in a dogbone shape, exhibited lower nominal stress levels below 500 MPa, similar to the stress-strain curves observed in this study. This similarity in nominal strain behavior suggests that the mechanical response of the specimens, despite their different origins (directly printed dogbones vs. extracted from printed cuboids), is influenced by the sintering process.

Although the specimens were obtained through different sample preparation methods, both displayed comparable nominal strain behavior. This observation suggests that the sintering process has a profound impact on the mechanical behavior of the material, regardless of the specific sample geometry. The fact that the nominal stress levels in both cases remained below 500 MPa indicates that the sintered 316L material may exhibit limitations in terms of its load-bearing capacity.

The extraction process from the cuboid shape may introduce additional stress concentrations or alter the microstructure near the extracted region, potentially affecting the fracture strength and stress-strain response.

5.9 Fracture Tests

5.9.1 Compliance Test

The compliance testing method, as mentioned before, although initially considered as a viable approach, encountered significant challenges that prevented the acquisition of meaningful data for the 316L sintered material under investigation. This section will discuss the specific challenges faced during the compliance tests and their implications in relation to the material's microstructure.

One of the main challenges encountered was the difficulty in achieving a controlled

crack initiation and propagation during the precracking process. The 316L sintered material exhibited a high level of ductility, as evidenced by the results obtained from the tensile tests. This inherent ductility made it challenging to initiate and propagate a controlled crack in a controlled manner. Various techniques were explored, including adjustments to the loading conditions and the implementation of specialized notch geometries, but achieving the desired level of crack control and reproducibility proved to be elusive.

The second challenge stemmed from the size of the specimens used in the compliance tests relative to the fixture. The specimens were relatively small, which made it impossible to attach conventional extensometers for direct crack mouth opening measurements. This limitation hindered the ability to accurately measure the strain and deformation of the specimens during the testing process. As an alternative, Digital Image Correlation (DIC) was employed to record the crack mouth opening displacement. However, due to the complex nature of crack propagation and the limitations of the DIC system, the measurements obtained were imprecise and unreliable. The inherent difficulties associated with accurately capturing the crack mouth opening displacement significantly hindered the effectiveness of the compliance method in obtaining precise and consistent results.

Despite the unsuccessful attempts to obtain meaningful data through compliance testing, valuable insights were gained from these challenges. The difficulties encountered during the precracking process highlighted the need for alternative methodologies and techniques that can better control crack initiation and propagation in highly ductile materials like 316L sintered. Furthermore, the limitations of using conventional extensometers due to the specimen size underscored the importance of developing specialized measurement techniques or adapting existing methods to accommodate small specimens.

These insights and lessons learned from the unsuccessful compliance tests provide a foundation for further exploration and potential future improvements.

5.9.2 Basic Procedure

Figure 4.9.1 illustrates the fracture behavior of the flat specimens, while Figure 4.9.2 presents the fracture behavior of the vertical specimens.

In Figure 4.9.1, the majority of the curves exhibit a consistent pattern characterized by a plateau phase. This plateau occurs at a load slightly above 500N and a displacement of approximately 1mm. The plateau phase represents a region where the specimen experiences relatively stable deformation without a significant increase in load. However, two specimens, 1BFB and 3BFT, deviate from this pattern. Specimen 1BFB reaches the plateau at a similar load but at an

earlier displacement compared to the other curves. Meanwhile, specimen 3BFT reaches the plateau at a load slightly above 300N and a displacement of 0.5mm. These deviations suggest that these two specimens may have different structural integrity. Beyond the plateau phase, the curves exhibit some dispersion, indicating variations in the behavior of the specimens as they approach fracture. The maximum point of each curve represents the point of ultimate load or failure for that particular specimen. The maximum load and displacement values differ across the specimens, indicating variations in their fracture strength and deformation capacity. For example, specimen 2BFT reaches a maximum load of approximately 900N at a displacement of 3mm, while specimen 1BFB fractures at a slightly higher load of over 1200N but at a displacement of 3.5mm. These variations highlight the influence of different factors, such as specimen notch size and printing orientation, on the fracture behavior and mechanical response.

Moving on to Figure 4.9.2, all the vertical specimens exhibit a similar plateau phase at a load slightly above 500N, but with variations in displacement ranging from 0.5mm to 1.5mm. The plateau phase represents a stage where the specimens experience limited deformation despite an increasing load. Beyond the plateau, the curves display variations in the maximum load and displacement values, indicating differences in fracture strength and deformation capacity among the specimens. For instance, specimen 1YVF fractures at a load of approximately 800N and a displacement of 3.2mm, while specimen 1YVB fails at a load of about 900N and a displacement of 2.4mm.

Figures 4.9.3, 4.9.4., and 4.9.5 depict the fracture behavior of specimens with different notch sizes. In these plots, similar observations can be made regarding the plateau phases and the maximum points of the curves. The plateau phase in each plot represents a stage of relatively stable deformation at loads slightly above 500N. The maximum load and displacement values vary among the curves, indicating differences in fracture strength and deformation capacity.

Figure 4.9.3 represents the fracture behavior of specimens with $R=0.25$ notch size. Similar to the previous plots, the curves exhibit a plateau phase between 0.5mm and 1.2mm at loads slightly above 500N, indicating stable deformation. Additionally, specimen 3BFT shows an additional smaller plateau phase at approximately 300N and 0.4mm. The maximum point of each curve provides insights into the fracture characteristics. For example, specimen 1BFB reaches its maximum load at approximately 3.5mm with a load slightly above 1200N. Specimen 1BVB fractures at about 900N and 2.5mm, while specimen 3BVF fails at 780N and 2.2mm. Moving on to Figure 4.9.4, which represents specimens with $R=0.5$ notch size. The curves in this plot display a similar plateau phase at loads slightly above 500N and displacements ranging from 0.6mm to 1mm. However, specimen 1YVF

exhibits a slightly higher plateau at 1.3mm with a load of 500N. Examining the maximum values of each curve, specimen 1YFB fractures at approximately 1190N and 4.6mm, specimen 1YVF fails at 800N and 3.2mm, and specimen 1YVB reaches a maximum load of almost 900N at 2.4mm. Similarly, specimens 2YVF and 2YFT exhibit different maximum load and displacement values, indicating variations in their fracture behavior.

Lastly, Figure 4.9.5 illustrates the fracture behavior of specimens with $R=1.00$ notch size. The curves in this plot display a similar pattern until the plateau phase, which occurs at a little above 500N and around 0.5mm displacement. The maximum load and displacement values provide insights into the fracture behavior of each specimen. For example, specimen 1GFB reaches its maximum load at approximately 1300N and 6.3mm, while specimen 1GVB fractures at about 1100N and 3.3mm. Similarly, specimens 2GFT and 1GFT exhibit different fracture strengths and deformation capacities.

Fracture toughness values were obtained for each notch size, and the average indicative values are presented in Table 4.9.2. As the notch size increases, the stress concentration at the notch decreases. This decrease in stress concentration leads to a higher resistance to crack propagation and, consequently, an increase in fracture toughness. The specimens with larger notch sizes ($R=1.0$) tend to exhibit higher maximum load and displacement values compared to those with smaller notch sizes ($R=0.25$ and $R=0.5$). This observation suggests that the specimens with larger notch sizes have a higher fracture toughness and, therefore, can withstand higher loads and deformations before fracture occurs. The plateau phases observed in the plots provide insights into the stability of deformation and the fracture toughness of the specimens. In the plots, the specimens with larger notch sizes ($R=1.0$) tend to have longer plateau phases compared to those with smaller notch sizes ($R=0.25$ and $R=0.5$). This longer plateau phase indicates a greater resistance to crack propagation and reflects the higher fracture toughness of the specimens with larger notch sizes. It is important to note that the fracture toughness values obtained in this study are merely indicative due to certain deviations from the standard protocol. The specimens were not pre-cracked as outlined in the basic procedure, and the measurement of crack propagation was not feasible. Therefore, the fracture toughness values should be interpreted with caution.

5.10 Fractography

Dogbone Fractured Surface

The primary focus is on the comparative visual representation of the fracture surfaces of specimens T1, T2, T3, and T4, before and after the tensile test. The aim is to identify the changes in fracture morphology and understand the effect of applied stress during the test.

Table 4.10.1 depicts the fracture surface of specimen T1, which was vertically printed. It shows a 45-degree crack that traverses the specimen, abruptly jumping two layers of the printing pattern. The appearance of the fractured surface suggests a lack of elongation. This observation raises questions about the mechanical properties of the printed and sintered 316L material, specifically its resistance to crack propagation and plastic deformation.

Table 4.10.2 showcases the fracture surface of specimen T2, also printed in a vertical orientation. In contrast to T1, T2 exhibits a ductile fracture with a 90-degree crack pattern. This type of fracture indicates that the material has undergone plastic deformation before failure, suggesting a certain level of ductility. The presence of plastic deformation suggests that the 3D printed and sintered 316L material possesses the ability to absorb energy during the tensile test.

Specimen T3, presented in Table 4.10.3, was printed in a flat orientation. Similar to T2, it displays a ductile fracture with a crack pattern resembling that of T2. The similarity in fracture morphology between T2 and T3 suggests consistent material behavior under similar loading conditions, despite the difference in printing orientation.

Table 4.10.4 represents the fracture surface of specimen T4, which was also printed in a flat orientation. It exhibits a crack pattern similar to T2 and T3. However, the crack in T4 is slightly closer to one of the sides of the dogbone specimen, deviating from the centrally located crack observed in T2 and T3. This variation in crack position may indicate the presence of local heterogeneity or stress concentration within the printed and sintered 316L material.

Etching on 3-Point Bending Fractured Surface

Figure 4.10.1 shows the etched crack on the vertical front of the fractured surface. The magnified view in Figure 4.10.2 provides a closer look at the crack's characteristics, allowing for a more detailed examination of its propagation pattern.

The presence of grains, although not clearly visible in Figure 4.10.3, suggests a polycrystalline structure, which is typical for materials like 316L. However, the limited visibility of the grains hinders a conclusive determination of the crack

type based solely on the etched surface.

Taking into account the material's properties, including its composition and microstructure, it is expected that 316L may exhibit intergranular fracture behavior.

SEM of 3-Point Bending Fractured Surface

The fractography analysis of the 316L material using SEM images provides valuable insights into the fracture behavior and ductility of the specimens. The SEM images were captured on the fractured surfaces of the vertical front, vertical back, flat front, and flat back specimens.

The SEM images of the vertical front specimens presented in Table 4.10.5, the image of specimen 1YVF shows the presence of dark spots indicating contamination on the fractured surface. Despite multiple cleaning attempts of the specimen, some level of contamination remains. Both specimens on this table exhibit a distinct layered pattern on the fracture surface, which corresponds to the printing direction, that was vertical in this case.

Table 4.10.6, which showcases SEM images of the vertical back specimens, the images provide a more apparent indication of ductility on the fracture surface. The presence of ductile features, such as dimples and elongated voids, suggests that the material underwent plastic deformation before failure. This observation is consistent with the expectation of 316L being a ductile material.

Examining the SEM image in Table 4.10.7, which corresponds to the flat front specimen, the fractured surface displays pores, but no distinct layered pattern is visible. This indicates that the fracture surface is not influenced by the printing direction and suggests a more isotropic fracture behavior.

Finally, Table 4.10.8 presents the SEM images of the flat back specimens. Similar to the flat front specimens, the fractured surfaces show the presence of pores, but no prominent layered pattern is observed. The presence of pores further suggests the material's ductile behavior, as the pores can act as nucleation sites for void formation during plastic deformation.

CONCLUSIONS

Throughout this thesis, the potential of producing stainless steel 316L using the MEAM technique while striving to maintain mechanical properties comparable to conventionally manufactured specimens was explored. The study involved the use of printed specimens with a composite filament composed of 316L powder particles and a polymer binder, followed by crucial post-processing steps such as debinding and sintering.

As this research is concluded, it is evident that the techniques employed in the MEAM and mechanical testing process hold promise but require further refinement. Despite the progress made, we encountered challenges leading to the presence of significant pores and rough surfaces in the printed specimens.

In our pursuit of overcoming these limitations, a comprehensive analysis was conducted, covering various aspects such as particle size distribution, surface roughness, defects and porosity distribution, grain size, microhardness, finite element simulations, fracture tests, tensile testing, and fractography.

Specimen Preparation

In conclusion, the preparation of dogbone specimens for tensile testing was executed with precision and attention to detail. Although minor discrepancies were observed in the thickness of some specimens, these variations are considered acceptable and are not anticipated to significantly affect the test results. Consequently, the extracted dogbone specimens were expected to provide reliable and representative data for subsequent mechanical tests.

The extraction process of 3-point bending specimens encountered more challenges. The cutting of these specimens proved to be a more complex task, resulting in a higher failure rate. Imperfections and variations in the notch sizes of the specimens were also observed, necessitating the replacement of some specimens. These chal-

allenges predominantly stemmed from inexperience and issues with the machine's cutting code.

Particle Size Measurement

The particle size measurements conducted revealed an average particle size of approximately 16 micrometers. However, smaller particles within the microscope's range of focus may have influenced this average, while larger particles located away from the focal plane might have been overlooked in the measurements.

Surface Roughness Evaluation

The surface roughness evaluation of the cuboids revealed notable differences in variation between the Top and Side surfaces, as well as between the different printed orientations.

Considering the different orientations of the cuboids, it is expected that the flat-printed cuboids would exhibit a higher degree of surface roughness variation compared to the vertical-printed cuboids. This is due to the larger surface area in contact with the build platform for flat-printed cuboids.

Defects and Porosity Distribution

The flat-printed specimen, representing the horizontal orientation, exhibited an overall lower density of pores compared to the vertical-printed specimen. It was observed that there is a slightly higher concentration of pores on the top surface of the flat cube. In contrast, the vertical-printed specimen displayed a distinctive pattern of porosity distribution. The side surfaces of the cube exhibited horizontal lines of pores. This pattern suggests that the printing process, particularly in the vertical direction, influenced the formation of these pore lines. Material deposition and consolidation in the vertical direction likely contributed to the development of these distinctive pore lines. The presence of deep lines on the Top of the vertical cube are likely related to factors encountered during the printing phase.

Grain Size Measurement

The average grain size values obtained from the analysis were approximately 38.7 μm for the flat specimen and 37.2 μm for the vertical specimen. These measurements indicate that both specimens have a similar microstructure with moderately sized grains.

Microhardness - Vickers

Lower microhardness values were observed near or on the pores, indicating that the presence of pores can influence the material's hardness. For the flat top specimens, the average HV2.0 microhardness values ranged from 104.71 to 111.16, indicating a certain level of hardness in the material. Slight variations were observed among different measurement points, suggesting localized differences in hardness. The average microhardness value for the flat specimens was approximately 10 units higher than that of the vertical back specimens, suggesting a potential difference in hardness between the two orientations. In the case of the vertical back specimens, the average HV2.0 microhardness values ranged from 97.17 to 98.94.

Finite Element Simulations

The simulation of a "Perfect" crack revealed a high σ value of 0.93830, indicating a significant stress concentration at the crack. Simulation 1, corresponding to a specific notch geometry, resulted in a higher Kt value of 7.21745, indicating substantial stress concentration at the notch.

Simulation 2, with a different notch geometry, yielded a lower Kt value of 4.94110, indicating stress concentration at the notch but to a lesser extent than in Simulation 1.

Simulation 3, with another notch geometry, resulted in a slightly lower Kt value of 4.33250, highlighting the influence of notch geometry on stress distribution and failure behavior.

In contrast, the simulation without any notch or crack (No Notch/Crack) exhibited a significantly lower Kt value of 2.94557, indicating reduced stress concentration and more uniform stress distribution throughout the material.

Tensile Test

The tensile tests conducted on four specimens, two obtained from vertically printed cuboids (T1 and T2) and two from flat printed cuboids (T3 and T4), reveal consistent elastic properties across all specimens.

T1 exhibits lower strength, fracturing at a nominal strain above 0.45 with a stress value of approximately 500 MPa. T2 fractures just below a nominal strain of 0.6, displaying higher stress than T1 but lower than T3 and T4. T3 fractures at around 0.65 strain with a stress level of almost 550 MPa, while T4 exhibits a similar fracture strain but with a slightly higher stress value, still below 0.7. Both T3 and T4 demonstrate higher strength compared to T1 and T2.

The specimens exhibit ductile behavior, resulting in premature yielding and reduced ultimate tensile strength compared to annealed AISI 316L. The reduction

in elastic modulus and offset yield strength further confirms this yielding behavior and reduced load-bearing capacity.

The high ductility and absence of significant local necking indicate uniform elongation during loading, supported by the total elongation at fracture exceeding the typical value. Porosity between strands due to insufficient overlap or temperature differences during printing hampers merging, but optimizing printing parameters and altering the sintering process may improve material uniformity and reduce porosity. The nominal stress levels remaining below 500 MPa indicate potential limitations in the material's load-bearing capacity. The extraction process from cuboids may introduce stress concentrations or alter the microstructure near the extraction region, affecting fracture strength and stress-strain response.

Fracture Tests

Compliance Test

The compliance testing method faced significant challenges in obtaining meaningful data. Difficulties in achieving controlled crack initiation and propagation due to the material's high ductility posed a major obstacle. Various techniques were explored, but reproducing desired crack control proved elusive.

The small size of the specimens prevented the use of conventional extensometers for accurate measurements, necessitating the use of Digital Image Correlation (DIC) for crack mouth opening displacement. However, the complex nature of crack propagation and the limitations of the DIC system resulted in imprecise and unreliable measurements.

Although the compliance tests did not yield meaningful data, they provided valuable insights. The challenges highlighted the need for alternative methodologies and techniques to control crack initiation and propagation in highly ductile materials like printed 316L.

Basic Procedure

The fracture behavior of the tested specimens reveals consistent patterns characterized by a plateau phase, representing stable deformation, at loads slightly above 500N and varying displacements. Deviations in fracture behavior are observed in certain specimens, indicating potential differences in structural integrity. Variations in maximum load and displacement values across specimens highlight the influence of factors such as specimen notch size and printing orientation on fracture strength and deformation capacity.

Similar observations are made in the fracture behavior of vertical specimens and specimens with different notch sizes.

Fractography

Dogbone Fractured Surface

The fractography analysis of the dogbone specimens provides valuable insights into the fracture behavior and mechanical properties of the material. Specimens T1 and T2, printed vertically, exhibit distinct fracture surface characteristics, including crack orientation and deformation patterns. In contrast, specimens T3 and T4, printed in a flat orientation, demonstrate fracture behavior similar to T2, suggesting that printing orientation may have a limited influence on the fracture characteristics of the material. The observed crack deviation in T4 highlights the potential role of local heterogeneity or stress concentration in fracture behavior.

Etching on 3-Point Bending Fractured Surface

The etching techniques provided valuable visual information on the crack characteristics and its correlation with the material's properties. The limitations in the visibility of grains on the etched surface hinder a definitive determination of the crack type on the grains. Further investigations involving advanced microscopy techniques and additional fracture analysis methods to confirm the presence of intergranular fracture or explore other potential fracture modes.

SEM of 3-Point Bending Fractured Surface

The SEM images of the fractured surfaces provide important insights into the fracture behavior and ductility of the 316L material. The presence of contamination on the vertical front specimens highlights the importance of thorough cleaning processes. The distinct layered pattern observed on the fracture surfaces of the vertically printed specimens corresponds to the printing direction. The absence of a layered structure on the flat specimens indicates a more isotropic fracture behavior. The presence of pores on the fracture surfaces, along with the observed ductile features, supports the expected ductility of the 316L material.

6.1 Further Work

While the conducted tests were well-executed overall, certain small details were not possible to achieve due to constraints or limitations. Therefore, future work should place a strong emphasis on fulfilling the requirements stipulated by the standards, in order to ensure the reliability and comparability of the obtained results.

It is crucial to ensure that future investigations adhere to the established standards for fracture testing. Specifically, the precracking phase should be correctly implemented according to standard procedures. This will enable the acquisition of accurate and reliable data for both procedures of fracture tests, ensuring the validity of fracture toughness calculations. Furthermore, it is recommended to employ not only Digital Image Correlation (DIC) but also a displacement extension clip to accurately measure the crack mouth opening displacement, thus enhancing the precision of the analysis. By addressing these areas, the research can provide more comprehensive insights into the behavior of the material and enhance the understanding of its mechanical properties and performance.

REFERENCES

- [1] Haidar Ramazani and Kami Abdolvahed. “Metal FDM, a new extrusion-based additive manufacturing technology for manufacturing of metallic parts: a review”. In: *Progress in Additive Manufacturing* 7 (2022). DOI: 10.1007/s40964-021-00250-x.
- [2] Dayue Jiang and Fuda Ning. “Physical-mechanical behaviors of stainless steel plate-lattice built by material extrusion additive manufacturing”. In: *Journal of Materials Processing Technology* 309 (2022), p. 117739. ISSN: 0924-0136. DOI: <https://doi.org/10.1016/j.jmatprotec.2022.117739>.
- [3] Saveria Spiller, Filippo Berto, and Seyed Mohammad Javad Razavi. “Mechanical behavior of Material Extrusion Additive Manufactured components: an overview”. In: *Procedia Structural Integrity* 41 (2022), pp. 158–174. ISSN: 2452-3216. DOI: 10.1016/j.prostr.2022.05.018.
- [4] Marius A. Wagner, Amir Hadian Tutu, and Sebastian Clemens Thomas Schweizer Mikel Rodriguez-Arbaizar Efrain Carreño-Morelli Ralph Spolenak Frank. “Fused filament fabrication of stainless steel structures - from binder development to sintered properties”. In: *Additive Manufacturing* 49 (2022), p. 102472. ISSN: 2214-8604. DOI: 10.1016/j.addma.2021.102472.
- [5] KS Boparai and R Singh. “Advances in fused deposition modeling”. In: *Reference module in materials science and materials engineering*. Elsevier, 2017.
- [6] Brian N Turner, Robert Strong, and Scott A Gold. “A review of melt extrusion additive manufacturing processes: I. Process design and modeling”. In: *Rapid Prototyping Journal* 20.3 (2014), pp. 192–204. ISSN: 1355-2546. DOI: 10.1108/RPJ-01-2013-0012.
- [7] T Kurose et al. “Influence of the Layer Directions on the Properties of 316L Stainless Steel Parts Fabricated through Fused Deposition of Metals.” In: *Materials* 13 (2020), p. 2493. DOI: 10.3390/ma13112493.

- [8] Aghnia Nurhudan Sugeng Supriadi Yudan Whulanza Agung Shamsuddin Saragih Ilmiah. “Additive manufacturing of metallic based on extrusion process: A review”. In: *Journal of Manufacturing Processes* 66 (2021), pp. 228–237. ISSN: 1526-6125. DOI: 10.1016/j.jmapro.2021.04.018.
- [9] Paramjot Singh et al. “Printability studies of Ti-6Al-4V by metal fused filament fabrication (MF3)”. In: *International Journal of Refractory Metals and Hard Materials* 91 (2020), p. 105249. ISSN: 0263-4368. DOI: 10.1016/j.ijrmhm.2020.105249.
- [10] P. Singh, V.K. Balla, and A. Gokce. “Additive manufacturing of Ti-6Al-4V alloy by metal fused filament fabrication (MF3): producing parts comparable to that of metal injection molding”. In: *Progress in Additive Manufacturing* (2021), pp. 593–606. DOI: 10.1007/s40964-021-00167-5.
- [11] Joamín González-Gutiérrez, Gustavo Beulke Stringari, and Igor Emri. “Powder injection molding of metal and ceramic parts”. In: *Some Critical Issues for Injection Molding*. 2012, pp. 65–88. DOI: 10.1007/978-3-642-24121-3_3.
- [12] Hasib Amm et al. “Rheology scaling of spherical metal powders dispersed in thermoplastics and its correlation to the extrudability of filaments for 3D printing”. In: *Additive Manufacturing* 41 (2021). ISSN: 2214-8604. DOI: 10.1016/j.addma.2021.101967.
- [13] Eduardo Meraz Trejo et al. “Compressive deformation analysis of large area pellet-fed material extrusion 3D printed parts in relation to in situ thermal imaging”. In: *Additive Manufacturing* 33 (2020), p. 101099. ISSN: 2214-8604. DOI: <https://doi.org/10.1016/j.addma.2020.101099>.
- [14] Zuoxin Zhou et al. “Additive manufacturing of heat-sensitive polymer melt using a pellet-fed material extrusion”. In: *Additive Manufacturing* 24 (2018), pp. 552–559. ISSN: 2214-8604. DOI: <https://doi.org/10.1016/j.addma.2018.10.040>.
- [15] Zuoxin Zhou et al. “Development of a direct feed fused deposition modelling technology for multi-material manufacturing”. In: *AIP Conference Proceedings* 1769.1 (2016), p. 020004. DOI: <https://doi.org/10.1063/1.4963614>.
- [16] Joanna Marczyk, Ksenia Ostrowska, and Marek Hebda. “Influence of binder jet 3D printing process parameters from irregular feedstock powder on final properties of Al parts”. In: *Advanced Powder Technology* 33 (2022). DOI: 10.1016/j.apt.2022.103768.

- [17] Ravi Enneti and Kevin Prough. “Effect of binder saturation and powder layer thickness on the green strength of the binder jet 3D printing (BJ3DP) WC-12%Co powders”. In: *International Journal of Refractory Metals and Hard Materials* 84 (2019). ISSN: 0263-4368. DOI: <https://doi.org/10.1016/j.ijrmhm.2019.104991>.
- [18] Vincent Demers and et al. “Material Extrusion Additive Manufacturing of Low-Viscosity Metallic Feedstocks: Performances of the Plunger-Based Approach”. In: (2022), pp. 1–28. DOI: <http://dx.doi.org/10.2139/ssrn.4184964>.
- [19] D. Ye et al. “Ni-loss compensation and thermomechanical property recovery of 3D printed NiTi alloys by pre-coating Ni on NiTi powder”. In: *Additive Manufacturing* 47 (2021). ISSN: 2214-8604. DOI: [10.1016/j.addma.2021.102344](https://doi.org/10.1016/j.addma.2021.102344).
- [20] N Shahrubudin, TC Lee, and R Ramlan. “An overview on 3D printing technology”. In: *Procedia Manufacturing* 35 (2019), pp. 1286–1296.
- [21] Zhiping Chen et al. “Influence of initial relative densities on the sintering behavior and mechanical behavior of 316L stainless steel fabricated by binder jet 3D printing”. In: *Materials Today Communications* 31 (2022), p. 103369. ISSN: 2352-4928. DOI: <https://doi.org/10.1016/j.mtcomm.2022.103369>.
- [22] Pawan Tyagi et al. “Reducing the roughness of internal surface of an additive manufacturing produced 316 steel component by chempolishing and electropolishing”. In: *Additive Manufacturing* 25 (2019), pp. 343–353. ISSN: 2214-8604. DOI: <https://doi.org/10.1016/j.addma.2018.11.001>.
- [23] Fulvio Lavecchia, Alessandro Pellegrini, and Luigi Maria Galantucci. “Comparative study on the properties of 17-4 PH stainless steel parts made by metal fused filament fabrication process and atomic diffusion additive manufacturing”. In: *Rapid Prototyping Journal* (2022). ISSN: 1355-2546. DOI: <https://www.emerald.com/insight/content/doi/10.1108/RPJ-12-2021-0350/full/html>.
- [24] Joamin Gonzalez-Gutierrez et al. “Additive Manufacturing of Metallic and Ceramic Components by the Material Extrusion of Highly-Filled Polymers: A Review and Future Perspectives”. In: *Materials* 11.5 (2018), p. 840. DOI: [10.3390/ma11050840](https://doi.org/10.3390/ma11050840). URL: <https://doi.org/10.3390/ma11050840>.
- [25] Qing Ju et al. “Thermoplastic starch based blends as a highly renewable filament for fused deposition modeling 3D printing”. In: *International Journal of Biological Macromolecules* 219 (2022), pp. 175–184. ISSN: 0141-8130. DOI: <https://doi.org/10.1016/j.ijbiomac.2022.07.232>.

- [26] Panagiotis Angelopoulos et al. “Manufacturing of ABS/expanded perlite filament for 3D printing of lightweight components through fused deposition modeling”. In: *Materials Today: Proceedings* 54 (2022), pp. 14–21. ISSN: 2214-7853. DOI: <https://doi.org/10.1016/j.matpr.2021.06.351>.
- [27] Mahrukh Sadaf, Mario Bragaglia, and Francesca Nanni. “A simple route for additive manufacturing of 316L stainless steel via Fused Filament Fabrication”. In: *Journal of Manufacturing Processes* 67 (2021), pp. 141–150. DOI: 10.1016/j.jmapro.2021.04.055.
- [28] Aboma Wagari Gebisa and Hirpa G Lemu. “Effects of Defects in Laser Additive Manufactured Ti-6Al-4V on Fatigue Properties”. In: *Procedia Manufacturing* (2019), pp. 331–338. ISSN: 2351-9789. DOI: <https://doi.org/10.1016/j.promfg.2019.02.047>.
- [29] Yuan-Hui Chueh et al. “Additive Manufacturing of Polymer-Metal/Ceramic Functionally Graded Composite Components via Multiple Material Laser Powder Bed Fusion”. In: *Journal of Manufacturing Science and Engineering* 142.5 (Mar. 2020). 051003. ISSN: 1087-1357. DOI: 10.1115/1.4046594. eprint: https://asmedigitalcollection.asme.org/manufacturingscience/article-pdf/142/5/051003/6518525/manu_142_5_051003.pdf. URL: <https://doi.org/10.1115/1.4046594>.
- [30] Peter Felfer et al. “Fused filament fabrication, debinding and sintering as a low cost additive manufacturing method of 316L stainless steel”. In: *Additive Manufacturing* (2019), p. 100861. ISSN: 2214-8604. DOI: 10.1016/j.addma.2019.100861.
- [31] J Holzer et al. “Properties for PIM feedstocks used in fused filament fabrication”. In: *World PM2016-AM-Deposition Technologies*. 2016.
- [32] Granta Design. *CES EduPack*. <https://www.grantadesign.com/products/edupack/>. Accessed in May, 2023. 2021.
- [33] H.R. Majidi et al. “Energy-based ductile failure predictions in cracked friction-stir welded joints”. In: *Engineering Failure Analysis* 102 (2019), pp. 327–337. ISSN: 1350-6307. DOI: <https://doi.org/10.1016/j.engfailanal.2019.04.066>. URL: <https://www.sciencedirect.com/science/article/pii/S1350630719302523>.
- [34] Sondre Olsøybakk Kolstad. “Structural Integrity of AISI 316L Fabricated via Material Extrusion Additive Manufacturing”. Supervisor: Seyed Mohammed Javad Razavi; Co-supervisor: Saveria Spiller. Master’s Thesis. Department of Material Science and Engineering, NTNU, June 2022.

- [35] *Standard Specification for Chromium and Chromium-Nickel Stainless Steel Plate, Sheet, and Strip for Pressure Vessels and for General Applications*. ASTM A240-21. ASTM International, 2021. URL: <https://www.astm.org/Standards/A240.htm>.
- [36] *Standard Specification for Seamless and Welded Austenitic Stainless Steel Tubing for General Service*. ASTM A269-21. ASTM International, 2021. URL: <https://www.astm.org/Standards/A269.htm>.
- [37] *Standard Specification for Stainless Steel Bars and Shapes*. ASTM A276-21. ASTM International, 2021. URL: <https://www.astm.org/Standards/A276.htm>.
- [38] Yagiz Kayali et al. “Effect of printing parameters on microscale geometry for 3D printed lattice structures”. In: *Materials Today: Proceedings* 70 (2022). DOI: 10.1016/j.matpr.2022.08.487.
- [39] *Standard Test Methods for Determining the Inclusion Content of Steel*. ASTM International, 2018. URL: <https://www.astm.org/Standards/E45.htm>.
- [40] *Standard Test Method for Determining Volume Fraction by Systematic Manual Point Count*. ASTM International, 2019. URL: <https://www.astm.org/Standards/E562.htm>.
- [41] *Standard Test Method for Quality Control of Porous Sintered Materials*. ASTM International, 2019. DOI: 10.1520/E2119-19.
- [42] H. Gong et al. “Comparison of Stainless Steel 316L Parts Made by FDM- and SLM-Based Additive Manufacturing Processes”. In: *JOM* 71 (2019). Received: 09 October 2018, Accepted: 25 October 2018, Published: 02 November 2018, Issue Date: 15 March 2019, pp. 880–885. ISSN: 1047-4838. DOI: 10.1007/s11837-018-3207-3. URL: <https://doi.org/10.1007/s11837-018-3207-3>.
- [43] James Allum, Andrew Gleadall, and Vadim V. Silberschmidt. “Fracture of 3D-printed micro-tensile specimens: filament-scale geometry-induced anisotropy”. In: *Procedia Structural Integrity* 28 (2020), pp. 591–601. ISSN: 2452-3216. DOI: 10.1016/j.prostr.2020.10.069.
- [44] Jehad M Nasereddin et al. “Development of a Simple Mechanical Screening Method for Predicting the Feedability of a Pharmaceutical FDM 3D Printing Filament”. In: *Pharmaceutical Research* 35 (2018). DOI: 10.1007/s11095-018-2432-3.
- [45] Ahmad Kholil et al. “The Effect of Orientation Angle and Layer Thickness on Surface Roughness of ABS Material on FDM”. In: *Materials Science Forum* 1057 (2022), pp. 3–10. DOI: 10.4028/p-m37s90.

- [46] Hassan Izadi Gonabadi et al. “Investigation of the effect of raster angle, build orientation, and infill density on the elastic response of 3D printed parts using finite element microstructural modeling and homogenization techniques”. In: *The International Journal of Advanced Manufacturing Technology* 118 (Jan. 2022). DOI: 10.1007/s00170-021-07940-4.
- [47] Tobias Rosnitschek et al. “Correlations of Geometry and Infill Degree of Extrusion Additively Manufactured 316L Stainless Steel Components”. In: *Materials* 14.18 (2021), p. 5173. DOI: 10.3390/ma14185173. URL: <https://doi.org/10.3390/ma14185173>.
- [48] Prusa 3D Printer. <https://www.prusa3d.com/>. Accessed: June, 2023.
- [49] Ultrafuse[®] 316L. <https://www.ultrafusefff.com/product-category/metal/ultrafuse-316l/>. Accessed: January, 2023.
- [50] Makino. *Kaspe Maskin AS, U6H.E.A.T. Makino wire EDM U6*. MTP - Workshop. Department of Mechanical and Industrial Engineering, NTNU. Kaspe Maskin AS.
- [51] *Standard Test Methods for Tension Testing of Metallic Materials*. 2016.
- [52] ASTM International. *Standard Test Method for Measurement of Fracture Toughness*. West Conshohocken, PA: ASTM International, 2008. DOI: 10.1520/E1820-08A. URL: <https://www.astm.org/Standards/E1820.htm>.
- [53] Inc. Hirox-USA. *Hirox rH-2000 digital microscope*. <https://www.hirox-usa.com/products/microscopes/rh-2000-digital-microscope/>. 2023.
- [54] *Hydrochloric acid*. Product information from Fisher Chemical. CAS number 7647-01-0. Fisher Scientific, 2023. URL: <https://www.fishersci.com/shop/products/hydrochloric-acid-37-w-v-aqueous-solution-3/p-243787>.
- [55] VWR International AS. *Nitric acid 60%*. Product datasheet. 2023. URL: <https://no.vwr.com/store/product/227-6097/salpetersyre-60>.
- [56] *Standard Test Methods for Determining Average Grain Size*. ASTM International, 2010. URL: <https://www.astm.org/Standards/E112.htm>.
- [57] Olympus Corporation. *Olympus BX53M optical microscope*. <https://www.olympus-lifescience.com/en/microscopes/upright/bx53m/>. 2023.

- [58] Dragan Adamovic and Fatima Zivic. “Hardness and Non-Destructive Testing (NDT) of Ceramic Matrix Composites (CMCs)”. In: *Encyclopedia of Materials: Composites*. Ed. by Dermot Brabazon. Oxford: Elsevier, 2021, pp. 183–201. ISBN: 978-0-12-819731-8. DOI: <https://doi.org/10.1016/B978-0-12-819724-0.00074-4>. URL: <https://www.sciencedirect.com/science/article/pii/B9780128197240000744>.
- [59] Mitutoyo Corporation. *Mitutoyo HM-200 Series Micro-Hardness Tester*. <https://www.mitutoyo.com/products/hm-200-series-micro-hardness-tester/>. 2023.
- [60] *MTS Criterion Model 42*. Manufacturer’s Manual. MTS Systems Corporation.
- [61] Inc. Correlated Solutions. *Vic-2D-v6 Digital Image Correlation (DIC)*. <https://www.correlatedsolutions.com/products/vic-2d/>. 2023.
- [62] A.R. Torabi. “Estimation of tensile load-bearing capacity of ductile metallic materials weakened by a V-notch: The equivalent material concept”. In: *Materials Science and Engineering: A* 536 (2012), pp. 249–255. ISSN: 0921-5093. DOI: <https://doi.org/10.1016/j.msea.2012.01.007>. URL: <https://www.sciencedirect.com/science/article/pii/S092150931200010X>.
- [63] Dassault Systèmes. *Abaqus*. <https://www.3ds.com/products-services/simulia/products/abaqus/>. Accessed early 2023. 2021.
- [64] *StepLab - Axial 20 kN Testing Machine*. Step Engineering S.r.l., Italy. Accessed early 2023. 2023.
- [65] *FEI · QUANTA 650 FEG · SEM*. Manufacturer’s website. Accessed in May, 2023. URL: <https://www.fei.com/products/sem/quanta-family/quanta-650/>.
- [66] ASTM International. *Standard Test Method for Microindentation Hardness of Materials*. ASTM International, 2017. URL: <https://doi.org/10.1520/E0384-17>.
- [67] MTS. *MTS - Criterion - Electromechanical Load Frame - 5 KN*. MTP - Fatigue, fracture and mechanical characterization. Department of Mechanical and Industrial Engineering, Gløshaugen Campus, NTNU. MTS Systems Corporation.

APPENDICES

PARTICLE SIZE MEASUREMENTS

Table A.0.1: Particle Size Measurements in micrometers.

	Values
	15.33
	12.9
	9.35
	18.09
	22.25
	14.88
	11.34
	23.22
	6.48
	22.28
	17.77
	6.80
	11.66
	16.80
	6.52
	16.88
	21.00
	25.18
	15.60
	23.24
	17.77
	9.40
	31.62
	15.92
Average:	16.345

ROUGHNESS EVALUATION

Values

The cuboids available for the roughness evaluation were two flat printed and 4 vertically printed cuboids.

Table B.0.1: Roughness Values, measured in micrometers.

Cube	Direction	RA1	RA2	RA3	RA4	RA5	<i>Average per Surface</i>	<i>Average per Cube</i>
F1	Axis_Y	28.7	27.9	33.4	23.8	25	27.76	
F1	Axis_Z	32.2	54	30.7	25.4	54.9	39.44	33.60
F2	Axis_Y	20.3	28.5	30.4	32	24.6	27.16	
F2	Axis_Z	37.8	20.1	33.3	21.4	27.7	28.06	27.61
V1	Axis_Y	28.4	20	31.8	26.7	26.6	26.70	
V1	Axis_Z	55.8	24.6	44.2	24.3	25	34.78	30.74
V2	Axis_Y	20.8	24	23.5	32.6	28.2	25.82	
V2	Axis_Z	52.1	27.8	22.2	28.1	21.1	30.26	28.04
V3	Axis_Y	21.7	22.9	31.8	23.8	26.6	25.36	
V3	Axis_Z	54.1	19.3	37.2	24.4	24.8	31.96	28.66
V4	Axis_Y	29.5	24.6	26.1	22.9	26.4	25.90	
V4	Axis_Z	23.1	29.2	24.3	23.9	35.5	27.20	26.55

F1

Table B.0.2: Roughness 3D image example for illustration purposes - 5 measures taken in different positions of the top of the cuboid printed flat number 1. The evaluation length used was 2.5 mm per each measure.

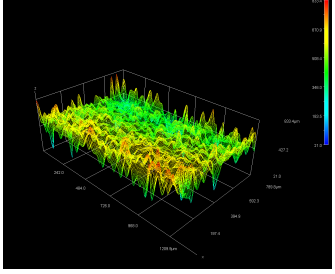
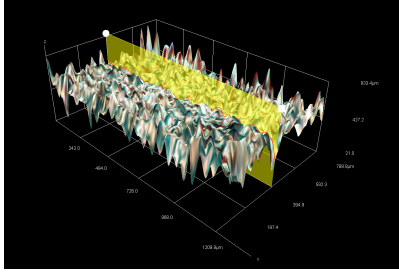
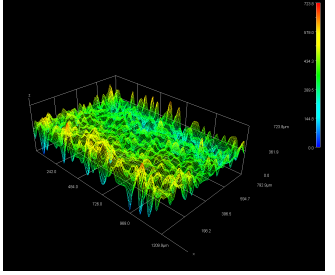
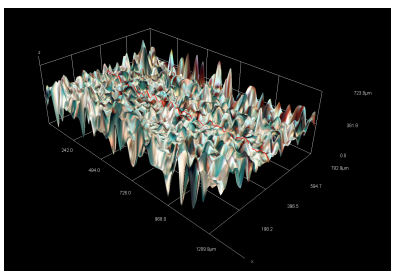
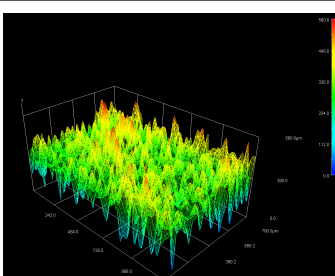
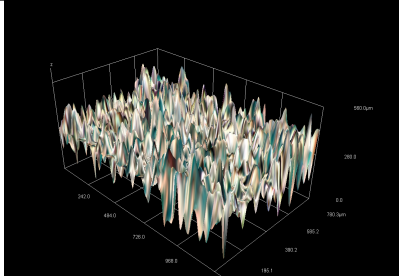
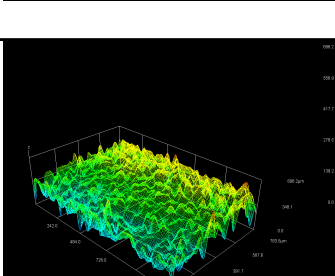
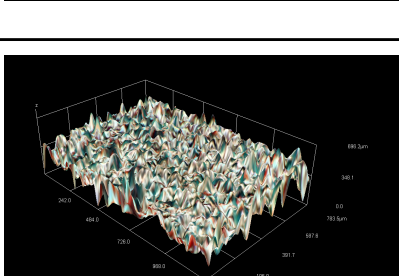
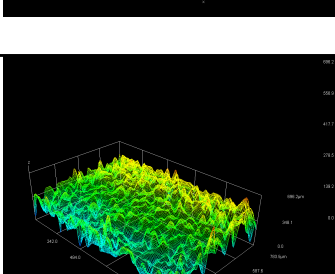
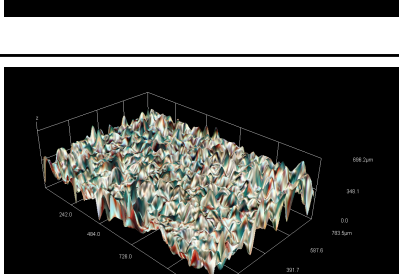
F1		
1		
2		
3		
4		
5		

Table B.0.3: Roughness Graphs example for illustration purposes - Cube F2.

F2	Graph
1	
2	
3	
4	
5	

APPENDIX

C

MICROHARDNESS - VICKERS

Table C.0.1: Vickers values on Flat Top Specimen, measured in micrometers.

Flat Top	Value	D1	D2
A1	76.7	213.7	226.1
A2	104.2	190.7	190.7
A3	103.9	190.3	191.6
A4	106.0	190.2	188.1
A5	104.8	188.1	188.1
A6	110.1	188.1	183.1
A7	106.3	187.1	186.5
A8	117.9	177.5	177.1
A9	110.1	183.6	183.5
A10	107.1	186.1	186.1
<i>Average:</i>	104.71		
B1	105.8	186.1	188.3
B2	112.2	181.8	181.8
B3	102.3	190.4	190.4
B4	106.9	186.3	186.3
B5	113.5	179.5	182.1
B6	107.6	184.3	187.0
B7	119.1	176.5	176.4
B8	113.8	180.5	180.5
B9	113.2	181.0	181.0
B10	117.2	178.3	177.5
<i>Average:</i>	111.16		
C1	104.7	188.2	188.2
C2	114.3	180.1	180.2
C3	113.7	180.6	180.6
C4	103.4	189.4	189.4
C5	110.1	183.6	183.6
C6	110.1	183.6	183.6
C7	113.2	182.2	179.8
C8	109.9	182.9	184.5
C9	112.5	179.2	183.8
C10	114.3	179.6	180.7
<i>Average:</i>	110.62		

Table C.0.2: Vickers values on Vertical Back Specimen, measured in micrometers.

Vertical Back	Value	D1	D2
A1	103.4	189.4	189.4
A2	79.6	215.9	215.8
A3	77.1	219.4	219.3
A4	68.0	233.6	233.6
A5	114.0	180.3	180.4
A6	107.7	185.5	185.7
A7	110.6	182.8	183.5
A8	111.3	181.9	183.2
A9	108.3	185.1	185.1
A10	91.7	201.1	201.1
<i>Average:</i>	97.17		
B1	82.2	212.4	212.4
B2	98.5	194.1	194.0
B3	113.0	181.2	181.2
B4	107.6	185.6	185.7
B5	107.9	185.4	185.4
B6	109.6	183.9	183.9
B7	108.8	182.2	186.9
B8	95.8	195.9	197.6
B9	83.2	211.1	211.1
B10	77.0	219.5	219.5
<i>Average:</i>	98.36		
C1	78.7	217.1	217.1
C2	102.3	190.4	190.4
C3	102.5	190.3	190.3
C4	97.2	195.3	195.3
C5	77.3	218.9	219.0
C6	107.8	185.5	185.5
C7	115.6	179.7	178.5
C8	107.5	185.4	186.2
C9	110.6	183.1	183.2
C10	89.9	203.2	203.1
<i>Average:</i>	98.94		

SIMULATIONS

Example:

If the maximum stress at the apex of the notch was found to be 100 MPa, and the stress in the specimen without the notch was 50 MPa, the stress concentration factor would be:

$$Kt = \frac{100MPa}{50MPa} = 2 \quad (D.1)$$



 **NTNU**

Norwegian University of
Science and Technology